Structural and Electrochemical Properties of Physisorbed and Chemisorbed Water Layers on the Ceramic Oxides Y_2O_3, YSZ and ZrO_2

Eva-Maria Köck[1], Michaela Kogler[1], Bernhard Klötzer[1], Michael F. Noisternig[2], Simon Penner[1,]*

[1]*Institute of Physical Chemistry, University of Innsbruck, Innrain 80-82, A-6020 Innsbruck*

[2]*Institute of Pharmaceutical Technology, University of Innsbruck, Innrain 52c, A-6020 Innsbruck, Austria*

*Corresponding author: simon.penner@uibk.ac.at, Tel: 004351250758003, Fax: 004351250758198

Abstract

The present study focuses on the adsorption and conduction behavior of H_2O and D_2O on the technologically important ceramic oxides YSZ (8 mol% Y_2O_3), ZrO_2 and Y_2O_3. For YSZ, a sequential dissociative water – "ice-like" layer - polymeric chained water – "liquid-like" water adsorption model for isothermal and isobaric conditions over a pressure range of 10^{-5} mbar up to 24 mbar and a temperature range from room temperature up to 1173 K could be established and experimentally verified, using a combination of *operando* Fourier-Transform infrared spectroscopy, *operando* electrochemical impedance spectroscopy and moisture sorption measurements. In contrast to highly hydroxylated YSZ and Y_2O_3, a high surface concentration of OH groups from water chemisorption is absent on pure monoclinic ZrO_2 at any temperature/pressure and thus, the ice-like and following molecular water layers exhibit no measurable protonic conduction. The characteristic changes of the related infrared bands could directly be linked to the associated conductivity and moisture sorption data. As the characterization of the chemisorbed and physisorbed water layers are imperative to a full understanding of (electro-)catalytically active doped oxide surfaces and their application in technology, the presented data provide the specific reactivity of these oxides towards water over a pressure/temperature parameter range extending up to e.g. solid-oxide fuel cell (SOFC)-relevant conditions. In due course, we show that the water layers even under these rather extreme experimental conditions play a key role in understanding the function of these materials. Furthermore, the reported data are supposed to provide an extended basis for further investigation of close-to-real gas adsorption or catalyzed heterogeneous reactions.

1. Introduction

Water chemistry on catalysts plays a key role in every efficient process[1-5], emphasized by the fact that a certain amount of mostly surface-bound water is always present in technical processes, e.g. upon energy generation in fuel cells. The amount of hydroxylation and even the amount of physisorbed water molecules on especially the oxide support of metal-oxide composite materials plays an important role for the overall activity of the system.[1] The actual contribution of OH-groups or other water-derived adsorbates on support and metal particle is currently an increasingly and intensively studied question,[6] as catalytic water activation on oxides in general is a cornerstone in catalyzed reactions like reforming reactions, the water gas shift reaction (WGSR)[7] or in water-assisted CO oxidation.[8-10] In this respect, water is an active participant of the catalytic reaction, either as a reactant or as a co-catalyst, and crucially influences e.g. the CO_2 selectivity in methanol or methane steam reforming reactions.[11, 12] Understanding the activation processes of adsorbed water molecules on different structural sites is thereby imperative. Besides a pure "catalytic" role, the adsorbed water molecules can also indirectly influence the material's properties. An instructive example is the well-known improvement of (especially surface) conduction processes by adsorbed water layers.[13, 14] In fact, for a range of mainly ceramic oxides, including Y_2O_3, ZrO_2 or Y_2O_3-doped ZrO_2, the "reduction" process in hydrogen has been basically shown to be limited to the surface layers and, thus, to the reversible removal of surface hydroxyl groups.[14] Naturally, this behavior is strongly dependent on the quality and quantity of the adsorbed water layers (i.e. if physisorption or chemisorption prevails) and the chemical nature of the adsorbing surface sites. Most importantly, these adsorbed water layers might also play a crucial role under comparably harsh experimental conditions (e.g. high temperatures) of relevant technological processes, where adsorbed water at first sight appears unlikely. A well-known example are solid-oxide fuel cells (SOFC's), to which fuel reforming or reformate mixtures (e.g. moist syngas) are fed.[15] However, despite the importance of understanding the role of the chemistry

and stability of these water layers stable at high temperatures and pressures, information in this respect is scarce. To eventually fill this knowledge gap, three representative "real" powder ceramic oxide materials with potential technological relevance have been chosen to directly highlight the water adsorption features as a function of surface chemistry. Y_2O_3, ZrO_2 and YSZ (stabilized by 8 mol% Y_2O_3) have therefore been selected, partly also because a large body of data of adsorption and material properties already exists, ranging from CO and CO_2 adsorption to reduction in CO or hydrogen.[16-19]

By combining *operando* Fourier-Transform infrared measurements, *operando* electrochemical impedance spectroscopy and dynamic moisture sorption investigations at different water partial pressures and temperatures it is, thus, possible to directly link the changes in surface chemistry caused by water adsorption to changes in the electrochemical behavior. In this respect, the resulting electrochemical response towards H_2O and D_2O at the respective application-oriented conditions, including isothermal and isobaric studies on pressed polycrystalline powder samples with water pressures between 10^{-5} mbar and ambient pressure, as well as a temperature range from room temperature up to 1173 K is studied. The pure oxides are thus investigated to clearly determine the contribution of the "isolated" oxidic components without the influence of metal particles and metal-oxide interfacial zones, which is increasingly necessary in order to disentangle the individual features of catalyst systems or complex materials in general. As a final note, more details of the structure of the adsorbed water layers on oxides have been jointly provided as an introductory chapter in the Results and Discussion section.

2. Experimental

2.1. Materials

Commercial powders of Y_2O_3 (yttrium(III) oxide, < 50 nm particle size, Sigma-Aldrich), ZrO_2 (zirconium(IV) oxide, 99.978%, Alfa Aesar), and YSZ (zirconium(IV)oxide, nanopowder, containing 8 mol % Y_2O_3 as stabilizer, Sigma Aldrich) were used as starting

materials. All samples were pre-treated by calcination at 1173 K in air and checked by XRD for structural changes upon annealing. To assure the same starting conditions and to guarantee that all samples are equally sintered for electrochemical impedance and Fourier-Transform infrared spectroscopy, the samples were heated in pure oxygen up to 1273 K with an extended isothermal period for 1 h before each experiment inside the respective setup. The surface areas after the pre-treatments were determined by BET nitrogen adsorption at 77 K (Quantachrome Nova 2000 Surface Area and Pore Size Analyzer) as 120 m^2g^{-1} (Y_2O_3), 32 m^2g^{-1} (YSZ), and 2 m^2g^{-1} (ZrO_2). Gases were supplied by Messer (O_2 3.5, He 5.0). The cooling trap temperature was ~153 K for O_2. D_2O was purchased from Sigma Aldrich (Deuterium oxide, 99.9 at.- % D).

2.2. FT-IR spectroscopy

FT-IR spectra were recorded in transmission mode on an Agilent Cary 660 spectrometer with a mid-infrared source and a DTGS detector. The powder samples were pressed into thin pellets using a pressure equivalent to 2 t on a 0.8 cm^2 area (sample diameter 10 mm, mass about 20 mg) and then subsequently placed inside a home-made *operando* reactor cell.[20] This cell provides an absolutely inert surrounding of the sample in the heated area. *In situ/operando* measurements up to 1273 K under flowing and static conditions can be performed. Vacuum conditions at a minimum pressure of $3\cdot10^{-7}$ mbar are possible. The window material BaF_2 allows access to wavelengths above 800 cm^{-1}. Experiments in flowing mode can be directly correlated with electrochemical impedance measurements and are performed using He as carrier gas. In static mode, water vapor can be added stepwise into the evacuated cell and is desorbed from a water reservoir that was degassed to remove dissolved CO_2. All reported spectra are corrected by the spectrum of the dry pre-oxidized oxide pellet at room temperature and under vacuum prior to exposure to water.

2.3. Electrochemical impedance spectroscopy

The *in situ/operando* impedance cell consists of an outer quartz tube with two inner quartz tubes to which the sample and the electrodes are attached. Heating was provided by a tubular Linn furnace and controlled by a thermocouple (K-element), located in the reactor about 5 mm downstream of the sample, and a Micromega PID temperature controller. The impedance was measured by an IM6e impedance spectrometer (Zahner Messsysteme), which provides data on the impedance and the phase angle of the current as a function of voltage. The powder samples were pressed into pellets with a pressure equivalent to 2 t on a 0.2 cm^2 area (sample diameter 5 mm, mass about 20 mg) and placed between two circular Pt electrodes forming a plate capacitor in mechanically enforced contact with the sample pellet.

For all temperature-programmed impedance measurements described in this article, an amplitude of 20 mV of the superimposed sinusoidal modulation voltage signal at an overall DC potential of 0 V and a frequency of 1 Hz were applied to the Pt electrodes, i.e. the impedance of the pellet was effectively measured in an electrochemically unpolarized state. In all temperature-dependent experiments the impedance modulus │Z│, obtained at 1 Hz modulation frequency, will be further referred to as "impedance".

Water vapor of 24 mbar was introduced by passing He (1 mL s^{-1}) through a water saturator at room temperature. For establishing a partial pressure of 4 mbar, the sublimation pressure of ice Ih was established, using a LN$_2$/EtOH cooling trap at ~ 270 K.[21] For the re-oxidation after moist treatments a LN$_2$/EtOH cooling trap at ~ 153 K was used.

Nyquist plots are obtained isothermally at a given temperature in a frequency range between 100 mHz and 0.1 MHz at the same amplitude of the superimposed sinusoidal voltage signal that is also used for the temperature-dependent impedance measurements. The real and imaginary part of the impedance are first measured from 1 kHz up to 0.1 MHz (within 14 s) and then from 0.1 MHz down to 100 mHz (within 4 m 24 s; total measuring time: 4 m 38 s) to check for time-dependent changes of the system during EIS. The obtained data have been fitted with the equivalent circuit model shown in Figure 9.

Arrhenius analysis was performed to determine the activation energies for certain temperature regions. From the temperature dependent EIS measurements the conductivity was calculated by taking the reciprocal of the impedance modulus value and plotting ln(conductivity) vs. the reciprocal of the reaction temperature. This conductivity is proportional to the sum of the total charge carrier concentration and not specific for a certain kind of charge carrier. Hence, in the more frequent cases of mixed charge carrier conductance, an "apparent" activation energy can be determined. This calculated activation energy is usually the weighted sum of several contributions, that is, if several activated processes occur simultaneously with unknown relative contributions, it may be possible only in exceptional cases to refer one specific E_A to a single charge transport process. Thus, we are able to identify qualitative changes in the E_A being clearly related to changes on the surface. The resistance values obtained from the fit of the Nyquist plots for the different processes were also transformed into conductivities. As in the case of the temperature dependent EIS measurements, "apparent" activation energies were calculated.

2.2. Sorption measurements

The dynamic moisture sorption experiments over a relative humidity (r.h.) range of 0% to 95%, at 25.0 °C, were measured on an automated multi-sample moisture sorption analyzer (SPS11, ProUmid GmbH & Co. KG), equipped with an analytical balance (Mettler Toledo GmbH) of 10 μg resolution. The processed dry air flow has an effective minimum partial water pressure/minimum relative humidity of 1%.

The samples (0.04 g to 0.5 g) were placed in aluminium dishes and loaded in the instrument, where the sample mass change was recorded in 10 minutes interval over a total period of 18.5 days. The measurement cycles are programmed in steps (in % r.h.): 40-30-20-10-5-0-5-10-20-30-40-50-60-70-80-90-95-90-80-70-60-50-40-30-20-10-5-0-5-10-20-30-40. The minimum time per step was 300 minutes and the maximum time was set to 48 hours. Once the samples reached the equilibrium condition (0.003% mass change within 60 minutes), the next step was

started automatically. Due to the dynamic atmosphere in the chamber and the fluffy powder state of Y_2O_3, all sample pans and the reference pan were covered with a lightweight sieve.

3. Results and Discussion

3.1. General remarks on the state of literature

Before discussing our results on YSZ, ZrO_2 and Y_2O_3, a brief summary of the actual state in literature is provided to establish a basic concept for a comparable discussion of water adsorption on different oxides.

As water adsorption is a very complex field of knowledge, a vast bulk of literature exists – including UHV studies, theoretical investigations and ambient pressure experiments on a huge variety of characterized adsorber materials like any kind of metals, oxides, salts or composites. Two comprehensive reviews concerning water adsorption available, one from Thiel and Madey[22] (1987) and from Henderson[6] (2002) exist. The latter gives a very detailed insight into possible structures and reactions of water with many metals, but also some oxide surfaces. Henderson roughly distinguishes between UHV and non-UHV conditions, which are divided into so called 'high-pressure' studies and liquid-solid interfacial studies. In the UHV community, the term 'high pressure' is referred to pressures below 10^{-6} mbar. Derived from Thiel et. al. and Henderson et. al., in general, clustering of water molecules is a wide-spread phenomenon, both under UHV conditions and at higher pressures. With increasing water coverage several distinguishable binding states of water can be identified. Henderson suggests three categories of adsorbed water from an energetic viewpoint: (i) the case of a much stronger water-surface interaction than water-water interaction (often leads to dissociation); (ii) a similar or equal water-surface to water-water interaction (first few water layer(s)) and (iii) water layers where the surface-water interaction plays a minor part. Figure 1 visualizes this generalized concept of distinguishable water 'layers'. Concerning category (i), especially on defective or chemically suitable surfaces water can dissociate and form surface OH-groups with usually two types of OH-groups present: terminal ("t"-OH, just one bond from the

8

oxygen atom to the surface) and multi-coordinated ("m"-OH, two or even more bonds to the surface) hydroxyl groups. The dissociation processes already take place under UHV conditions. The initial formation or the general presence of hydroxyl groups enhances further adsorption of water due to favored binding of water molecules via hydrogen bonds. The first "physisorbed" water layer (category (ii)) and, depending on the substrate, also a few more layers, respectively, are structurally "ice-like" (i.e. restricted in terms of molecular degrees of freedom) due to the "pinning" influence of the surface. This ice-like water layer is bonded extremely strongly (although it is "only" molecularly adsorbed = physisorbed) and shows totally different adsorption kinetics and conduction mechanisms compared to the layers above. Depending on the surface, adsorption of the ice-like layer takes place under non-UHV conditions. Applying even higher pressure, more physisorbed water layers are present (category (iii)). These water molecules with a greater distance to the surface tend to be less structured and also diffusion of H-atoms (Grotthuss mechanism, proton hopping between randomly adsorbed water molecules[13]) becomes more likely, which in literature is often referred to as "polymeric chained" or "poly-nuclear"[23] water due to the typical network of structured hydrogen bonds in this layer.

An example, which is in good correlation with the concept in Figure 1, is the structural composition of water clusters on TiO_2[24]. The authors claim that every water molecule can form four hydrogen bonds at maximum – two as hydrogen bond acceptor (O atom) and two as hydrogen bond donor (H atom). The number of intermolecular hydrogen bonds consequently strongly influences the electronic/binding state of the molecule, especially if the regarding water molecule acts as a hydrogen donor. The main part of water molecules in the "bulk" of the cluster can be viewed as polymeric chained H_2O molecules. In contrast, the outside spherical part of a "free" cluster is formed by water molecules with their H atoms outside of the cluster, leading to a weaker influence of hydrogen bonding to its chemical state. The first (ice-like) water layer on the surface of the oxide is again set apart insofar as the water

molecules are only hydrogen-bonded to the upper layers with their electronic state being also strongly influenced by the bond to the oxide surface. The presence of chemisorbed hydroxyl groups does also strongly influence the binding of the first physisorbed water layer.

At water pressures near the saturation vapor pressure of water, an additional category of adsorbed water (comparable with condensation) should be defined: a from now on called "liquid-like" phase, where diffusion of whole water molecules is possible (Figure 1).
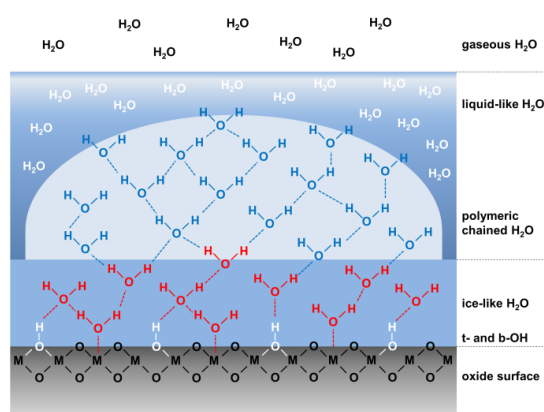

Figure 1: Generalized structural concept of water adsorption on an oxide surface.

In this study, especially with respect to the general energetic concept of water adsorption, FT-IR, dynamic moisture sorption and EIS measurements on ZrO_2, YSZ and Y_2O_3 were performed. The data are subsequently critically discussed in how far the quite generalized concept in Figure 1 is adaptable to the investigated oxides. Thus, to give the reader a better context, the aim of the experiments will be discussed in the beginning of each further section. Except from the structural properties of the adsorbed water, the status of the adsorbing substrate should also be discussed critically. The major part in literature providing detailed structure information of adsorbed water and forming the major focus in the Henderson review is single crystals. Oxides, especially in powder form, are rarely investigated, with the exception of TiO_2, SiO_2 and MgO. Details about water adsorption/hydroxylation on ZrO_2 are summarized in a review by Kouva et. al.[23]. The core point of the latter is that not only the total amount of hydroxylation but also the chemical nature of the hydroxyl groups are extremely

dependent on the pre-treatment of the oxide. Also the molecular adsorption of water – concerning amount and binding properties – is drastically dependent on the pre-treatment. The crucial parameter is the temperature, directly related with surface area, defect sites, particle size or predominant crystalline surfaces. Thus, also the concentration of dissociation or other binding sites, OH-concentration and type of OH groups are affected.

In our case the oxides are used as pressed powder samples (pre-)treated under SOFC relevant conditions (i.e. temperatures up to 1273 K). Upon comparing a single crystal with a powder sample there are additional parameters to consider. In general, the conducted measurements are based on comparably large-scale analytical techniques gathering data of the whole sample surface. As the surface area depends on several parameters of the oxides' pre-treatment, the samples were exclusively pre-treated in LN_2/EtOH dried O_2 up to 1273 K leading to controlled sample annealing and sintering, suppressing a high amount of remaining defects. The resulting "fixed" specific surfaces represent a realistic structurally invariant state, being the actual state of the oxides after pre-sintering under realistic conditions. We are aware of the fact that the surface of ZrO_2 (2 m^2g^{-1}) is much lower than the ones of YSZ (32 m^2g^{-1}) and Y_2O_3 (120 m^2g^{-1}). Polycrystalline powder samples might also offer structurally distinct adsorption sites (certain distribution of terminal crystallographic planes, under-coordinated sites at corners and edges, lattice dislocations, stacking faults or grain boundaries), which are absent on well-defined single crystals.

The adsorption of D_2O was additionally comparatively studied to H_2O adsorption since H/D exchange is a common method to clarify reaction mechanisms/kinetics[23] and the D_2O-related differences in adsorption properties or conduction effects provide valuable additional information.

3.2. FT-IR spectroscopy

As for isothermal experiments the lowest applied pressure is 10^{-5} mbar and the samples are pre-treated in dry O_2 (LN_2/EtOH trap) up to 1273 K, the surface starting state most likely

already provides a certain amount of hydroxylation (maximum of chemisorption on the annealed surface) and at maximum, very few physisorbed water molecules. The pressure of water vapor can be exactly controlled between 10^{-3} mbar and 24 mbar. Thus, it is possible to evaluate the water uptake starting from the ice-like layer up to the increasing amount of polymeric chained water layers. The highest applied water vapor pressure is 24 mbar (saturation vapor pressure of water at room temperature), which creates a multilayer water-covered surface up to liquid-like layers of water. With this setup, the energetic binding strength and correlated order of the water molecules in the different previously defined adsorption categories is directly expressed by the vibrational band of the respective O-H bond.
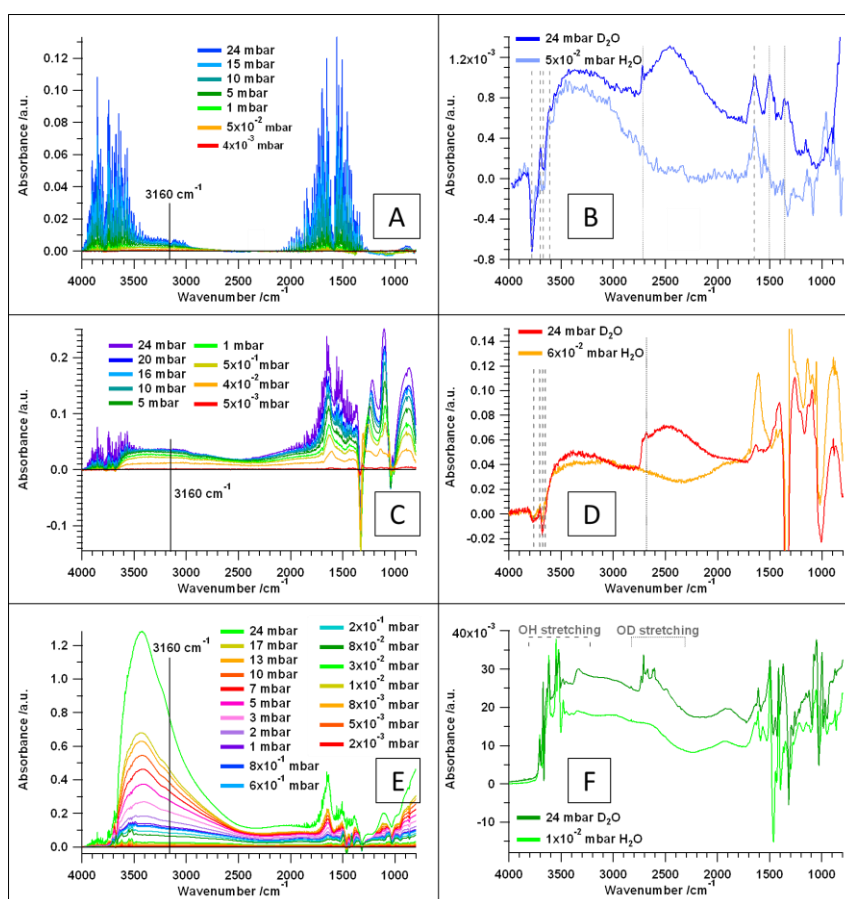

Figure 2: Isothermal FT-IR measurements of ZrO_2 (A) and (B), YSZ (C) and (D) and Y_2O_3 (E) and (F). (A), (C) and (E): experiments in pure H_2O vapor pressures from $\sim 10^{-3}$ mbar up to

24 mbar at room temperature; (B), (D) and (F): comparison of ~24 mbar D_2O vapor and ~ 10^{-2} mbar H_2O vapor.

Figure 2 shows an overview of the different water pressures on (A) ZrO_2, (B) YSZ and (C) Y_2O_3. On ZrO_2, signals for gaseous water are predominant at low pressures and the signals for adsorbed water are largely obscured by the strong $H_2O(g)$ bands. A definitive interpretation is possible at pressures below $1 \cdot 10^{-1}$ mbar, where the signals for gas phase water are not screening the bands of adsorbed water. A spectrum of ZrO_2 in $5 \cdot 10^{-2}$ mbar H_2O is displayed in Figure 2B in comparison to a spectrum of ZrO_2 in 24 mbar D_2O. The first distinct differences are two negative peaks at 3780 cm^{-1} and 3670 cm^{-1}. As a negative peak in a ratio spectrum indicates the change of a feature of the sample that was saved with the background spectrum, a change can be an actual removal/reaction of the regarding feature or just a change in the bond-length changing the position of the infrared band. The above mentioned negative signals are typical for the t-OH (3780 cm^{-1}) and m-OH (3670 cm^{-1}) groups of monoclinic ZrO_2.[23, 25-28] At starting conditions, where the background of the oxidized pellet was taken in vacuum of 10^{-5} mbar, there are already OH-groups present at the surface. If additional water molecules adsorb via hydrogen bonds to these hydroxyl species, the binding state of the H-O-bond changes leading to negative peaks in the ratio spectrum. The bands are red-shifted to 3700 cm^{-1} and 3610 cm^{-1} representing the first surface-near layer (consisting of OH and ice-like structured water molecule network). This is supported by Kouva et. al.[23] but also by studies on other oxides like Fe_2O_3 [29] and TiO_2[24,30]. The broad feature between ~ 3600 – 2800 cm^{-1} indicates H-bonded water und thus, both the ice-like layer and polymeric chained water with a comparably low impact on the oxide surface. The broadness of this feature is due to several possible OH bond-lengths/strengths being in a more dynamic intermolecular interaction as compared to the structurally "fixed" species at lower amounts of adsorbed water. Obviously, the wavenumber region above 2800 cm^{-1} contains a lot of information, but also below 1700

13

cm^{-1} distinct changes in the spectra, caused by water, are present. The peak at 1645 cm^{-1} can be assigned to the $\delta(OH)$ bending of physisorbed (multilayer, polymeric chained) water[24, 30]. As in the OH stretching region, negative peaks (below 1400 cm^{-1}) could be assigned to isolated OH groups, but in the case of ZrO_2 these signals are ill-defined at low pressures and the signals for gaseous water do interfere strongly at pressures higher than 10^{-2} mbar.

The comparison of H_2O and D_2O adsorption on ZrO_2 is shown in Figure 2B. Although the purity of the used D_2O is 99.9%, a small contamination with water could not be avoided. In fact, a pressure of $5 \cdot 10^{-2}$ mbar H_2O resembles the effect of H_2O in 24 mbar D_2O. Upon increasing the pressure of D_2O (not shown here), at first, only signals for the H_2O impurities are visible (up to a pressure range of 10^{-2} mbar) before H_2O saturation signals for D_2O arise. For H_2O this includes the exactly same negative signals for the t-OH (3780 cm^{-1}) and m-OH (3670 cm^{-1}) groups which are shifted to peaks at 3700 cm^{-1} and 3610 cm^{-1} along with the broad feature between 3600 cm^{-1} and 2800 cm^{-1} and a $\delta(OH)$ peak at 1645 cm^{-1}. The additional signals for adsorbed D_2O are a sharp peak for OD-stretching at 2720 cm^{-1} (ice-like D_2O near the surface), a broad feature (polymeric chained D_2O) from 2710 cm^{-1} to ~1960 cm^{-1} and $\delta(OD)$ vibration peaks at 1502 cm^{-1} and 1360 cm^{-1}.

Isothermal water adsorption on YSZ is shown in Figure 2C. In comparison to the experiment on ZrO_2, there are much more changes in the infrared spectra visible. In principle, more water can be adsorbed, since the relative changes in the spectra of YSZ are much more pronounced, especially in the $\delta(OH)$ region. The absorbance in Figure 2 is not normalized to the specific surface area and thickness of the sample pellet, but for a better comparability, this was done in in Figure 3. Nevertheless, although the specific surface area of the used YSZ is higher than for the used ZrO_2, the capacity of water adsorption is higher for YSZ (see also discussion below). Doping monoclinic ZrO_2 with 8 mol% Y_2O_3 leads to a tetragonal phase with an increased amount of surface defects leading to an increased amount of dissociation sites for water. Thus, at the starting conditions of the isothermal experiment, there are more OH groups

14

present on YSZ than on ZrO_2, strongly influencing/promoting further water uptake due to the increased polarity of the surface and the possibility of stabilization via hydrogen bonds.

In the wavenumber region for OH stretching modes there are similar changes taking place as on pure ZrO_2. The negative peaks for isolated OH-groups are at 3770 cm^{-1} and 3682 cm^{-1}. These signals are red-shifted to 3701 cm^{-1} and 3656 cm^{-1}. A noticeable difference between ZrO_2 and YSZ is the fact that on ZrO_2 the signal for the t-OH is more pronounced and on YSZ m-OH seems to be the more frequent species. The obvious explanation is again the doping with Y_2O_3, since on every defect near an Y^{3+} center, a m-OH group can be formed.

The signal for O-H bending for polymeric chained water is shifted with increasing pressure from 1605 cm^{-1} (up to 10^{-1} mbar) to 1636 cm^{-1} (24 mbar). There are significant negative peaks at 1330 cm^{-1} and 1038 cm^{-1}, which can be referred to $\delta(OH)$ vibrations of the isolated hydroxyl groups. The evolution of the other peaks is quite complex during pressure increase (see also Figure S2): at pressures below $2 \cdot 10^{-1}$ mbar there are peaks at 1305 cm^{-1}, 1138 cm^{-1}, 1224 cm^{-1} and 1052 cm^{-1}. Interestingly, at $2 \cdot 10^{-1}$ mbar a change in the spectra is observed. As already mentioned, the $\delta(OH)$ peak for polymeric chained water is constantly shifted to higher wavenumbers above this pressure and the other remaining peaks are also constantly changing to 1217 cm^{-1} and 1104 cm^{-1} at 24 mbar. This indicates a structurally quite more complex layer growth than on ZrO_2. Although a detailed discussion of every peak cannot be offered at this point, the explanation for the changes is the influence of Y in YSZ compared to pure ZrO_2. As mentioned above, doping of ZrO_2 with 8 mol% Y_2O_3 does certainly not only change structural parameters like the crystallographic phase (monoclinic to tetragonal) and specific surface area (2 m^2g^{-1} to 32 m^2g^{-1}), but also the chemical adsorption behavior towards water due to the introduction of defects/more dissociation sites and the creation of additional Y-binding sites.

D_2O adsorption on YSZ (Figure 2D) leads to an additional O-D stretching peak at 2680 cm^{-1} for ice-like D_2O and a broad feature from 2670 cm^{-1} to ~1950 cm^{-1}. The signals for the H_2O impurity are comparable to the one of $6 \cdot 10^{-2}$ mbar H_2O.

Since the changes in the delta OH/OD region are already quite pronounced for H_2O adsorption, it was not possible to determine any specific peaks for a delta O-D mode, due to the fact that the fingerprint in this region looks very similar to the one in $6 \cdot 10^{-2}$ mbar pure H_2O.

Water adsorption on Y_2O_3 is shown in Figure 2E. Y_2O_3 is a very hygroscopic oxide which is reflected in the infrared data for water adsorption. The modes of adsorbed water are much more complex than for the other two oxides indicating a variety of binding sites or discrete adsorption states. In fact, Y_2O_3 has a much larger specific surface area than the other two oxides ($120 \ m^2g^{-1}$), increasing the possibility of a higher number of separated H_2O islands or OH groups/dissociation sites. Additionally, the dynamic sorption measurements in section 3.3 prove that incorporation of water molecules forming extended hydroxide domains takes place. Thus, already from the infrared data we can state that the general concept of water adsorption on oxides derived from literature in section 3.1 is not valid for Y_2O_3, which rather becomes hydrolysed towards its hydroxide, along with crystal water inclusion. In fact, water uptake is more comparable to e.g. the CaO vs. $Ca(OH)_2$ system. One negative peak at 3678 cm^{-1} can be referred to a multi-coordinated OH group on Y_2O_3. Already at a pressure of $2 \cdot 10^{-3}$ mbar, there are several strong peaks at 3706 cm^{-1}, 3672 cm^{-1}, 3619 cm^{-1}, 3549 cm^{-1}, 3524 cm^{-1} and 3480 cm^{-1}. Comparing with $Ca(OH)_2$, peaks above ~ 3600 cm^{-1} can be referred to dissociated water and discrete peaks below ~ 3600 cm^{-1} to crystal water.[31] These peaks increase strongly up to a pressure of 1 mbar (compare also Figure S3), where the broad water feature gets significant and further increase of the water pressure leads to a superposition of most of the distinctive peaks by the polymeric chained water feature from 3660 cm^{-1} to ~2500 cm^{-1} including a distinctive peak at 3690 cm^{-1} (representing structured water layers near the surface). The broad OH feature for adsorbed water at 24 mbar it extremely pronounced in comparison to the peaks of gaseous water, indicating a very strong water uptake up to high pressures.

16

Also in the region for δ(OH) vibrations there are several peaks observed especially at pressures below 1 mbar. The most distinctive are at 1495 cm^{-1}, 1413 cm^{-1}, 1055 cm^{-1}, 1463 cm^{-1} (negative) and 1317 cm^{-1} (negative). None of these peaks does match any peaks of the other two oxides. The mode for the δ(OH) vibration of polymeric chained water can be assigned to 1644 cm^{-1} at a pressure of 24 mbar.

D_2O adsorption on Y_2O_3 is as complex as H_2O adsorption. Similar to the other oxides the spectra in 24 mbar D_2O can be compared to a H_2O pressure of $1 \cdot 10^{-2}$ mbar. Besides the above mentioned OH signals for the H_2O impurities there are distinct O-D stretching modes at 2732 cm^{-1}, 2709 cm^{-1}, 2670 cm^{-1}, 2620 cm^{-1} and 2607 cm^{-1}. Like on YSZ, the delta O-D modes are hard to distinguish because of the strong superimposition with the water delta OH signals.

An additional comment on the high amount and reactivity of the OH groups on Y_2O_3 should be added in comparison to other adsorption studies with CO and CO_2.[16] In general, a certain amount of hydroxylation is necessary for a good catalytic activity, but as also stated by Moreau et al.[4], too many hydroxyl groups can cause an activity loss. This is corroborated by the fact that on Y_2O_3 carbonates (chemisorption of CO_2) cannot be removed in oxidative atmosphere up to 1173 K.[19] All assignable vibrations on ZrO_2, YSZ and Y_2O_3 are jointly summarized in Table S1.

From the FT-IR data, more information can be obtained by plotting the relative height/absorbance of the broad water feature against the partial pressure. Since the water gas phase modes increasingly screen this analysis at pressures $> 10^{-2}$ mbar especially on ZrO_2, this was done at a wavenumber of 3160 cm^{-1} where the signal intensity of gaseous water is zero (Q-branch of the first overtone of the delta rotational-vibrational mode[32], see magnification in Figure S1). The resulting trend is plotted in Figure 3. Note that the data are shown up to a p/p_0 value of 0.6 due to the fact that the liquid-like layers do not contribute to the infrared signal. For the direct comparison of the oxides, the absorbance values were

normalized to the specific surface area and the sample mass (directly correlated with the thickness of the pellet).
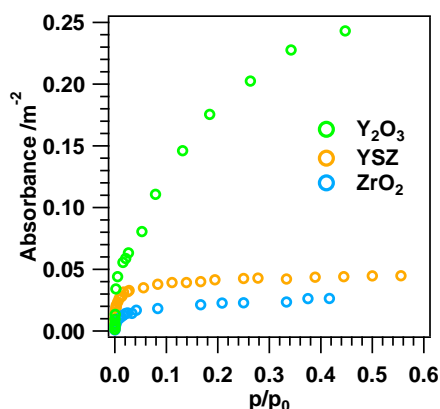

Figure 3: Plot of the absorbance at 3160 cm^{-1} of ZrO_2 (blue), YSZ (yellow) and Y_2O_3 (green) normalized to sample mass and surface area.

At pressures below ~ 1 mbar ($p/p_0 = 0.04$) on all samples a drastic increase of the absorbance at 3160 cm^{-1} is observed and for ZrO_2 (Figure 3, blue dots) and YSZ (Figure 3, yellow dots) any further increase of the water vapor pressure has a reduced impact on the absorbance at this wavenumber. Two processes of water adsorption can be derived from this plot: the irreversible growth of the ice-like water layer expressed by the first steep increase, and, once this layer reaches its maximum, only the adsorption of the polymeric chained water molecules is observed. In this context we also refer to the correlation with the dynamic sorption measurements in section 3.3. The adsorption behavior of Y_2O_3 is distinctly different from that of the other two oxides. Its hygroscopic nature is expressed especially by the fact that water molecules are incorporated, and thus, evaluating the data at 3160 cm^{-1} (Figure 3, green dots) leads to a very different course of the absorbance as for the other two oxides.

Figure 3 again reflects the general capacity of water uptake for the oxides: Y_2O_3 > YSZ > ZrO_2. Comparing YSZ and ZrO_2, not only with respect to the total amount of adsorbed water but also the capacity of molecules in the ice-like layer, the steep increase for the lower partial pressures is higher for YSZ than for ZrO_2.

18

Comparing the infrared data of the three oxides to the generalized concept in Figure 1, it is obvious that distinct differences concerning H_2O adsorption are observed. Due to the fact that on Y_2O_3 an extended hydroxide layer along with crystal water is formed, the adsorption on this oxide cannot be directly compared to ZrO_2 and YSZ, but this process is also crucially different to the generalized adsorption of water stated in section 3.1. For ZrO_2 and YSZ, the concept is valid to a certain extent, but the fact is striking that the amount of active sites – and thus the actual amount of already dissociated OH-groups – on these oxides, which is strongly influenced by doping ZrO_2 with Y_2O_3, affects the growth of both the ice-like layer and the subsequent polymeric chained layers.

3.3. Dynamic moisture sorption experiments

For the dynamic moisture sorption experiments the relative humidity is set by mixing a flow of dry air with a flow of water saturated air. The minimum moisture of the dry air flow is 1 % relative humidity, implying that, although the oxide powders were pre-oxidized up to 1273 K, the surface of the particles provides not only hydroxyl groups but also a full occupation of the ice-like layer. In contrast to the FT-IR setup, the moisture sorption setup provides a dynamic atmosphere. This method evaluates roughly the state of the samples above the bend in the plot of the absorbance at 3160 cm^{-1} versus the partial pressure in Figure 3.
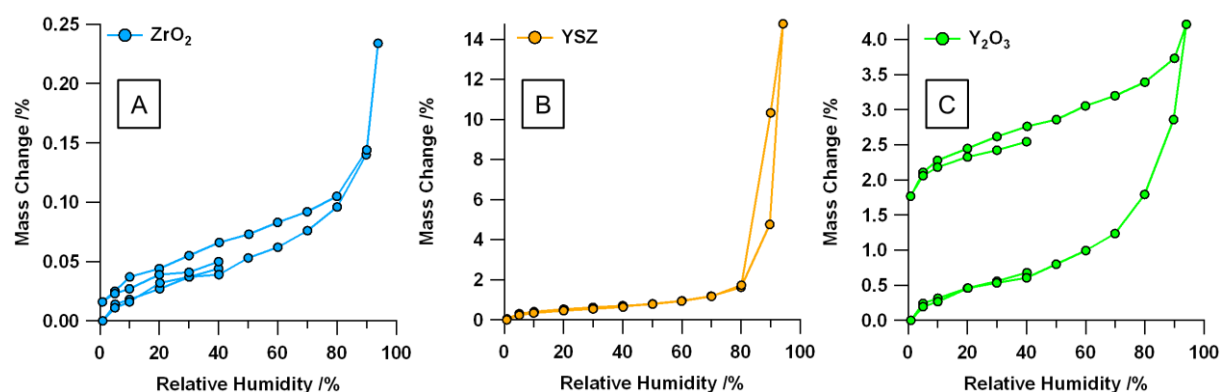

Figure 4: Dynamic moisture sorption measurements of ZrO_2 (A), YSZ (B) and Y_2O_3 (C).

For ZrO_2 (Figure 4A) and YSZ (Figure 4B) a reversible adsorption-desorption cycle is deduced, in contrast to Y_2O_3. The hysteresis over the whole relative humidity range in Figure 4C together with the FT-IR data for Y_2O_3 strongly indicates that water is more or less irreversibly incorporated into the crystal structure. Thus, the observed uptake of at maximum ~ 4 % mass change on Y_2O_3, which is quite low compared to YSZ, is just 'the tip of the iceberg'. On YSZ, as well as on ZrO_2, no uptake of crystal water can be observed. According to Sing et. al.[33] the course of the moisture sorption on YSZ is HI-type. The shape of this loop is often associated with porous materials known to consist of agglomerates (or compacts of uniform spheres). Especially on YSZ, capillary condensation is pronounced above 80% relative humidity, where the mass change increases from ~ 1.5 % to 13.3 %. In comparison, the mass change on ZrO_2 at 80 % relative humidity is ~ 0.1 % and the maximum mass change on ZrO_2 is 0.23 %. The sorption data are again reflecting the general findings of the FT-IR data in 3.2: the general capacity to adsorb water is sufficiently increased for YSZ in comparison to ZrO_2, which cannot be derived only by the different surface areas but actually by the amount of OH groups on the surface. Calculated from the mass change in the sorption data and the known surface area, the uptake of water can also be expressed by mol H_2O per m^2 oxide surface (see Figure 5A).
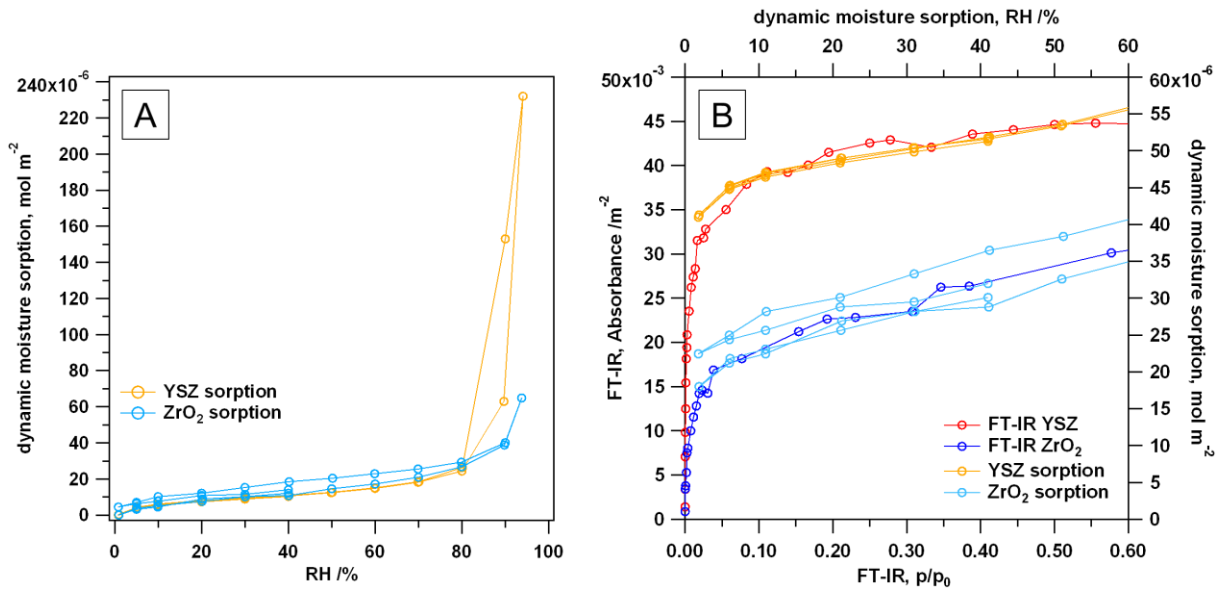
Figure 5: (A) Dynamic moisture sorption measurements of ZrO_2 (blue), YSZ (yellow) in mol H_2O per m^2 oxide surface; (B) determination of the 'offset' for the sorption experiment compared to the FT-IR evaluation at 3160 cm^{-1}.

Comparing the uptaken mol H_2O per m^2 oxide surface of YSZ and ZrO_2, Figure 5A proves that the water uptake per square meter available surface is actually the same up to 80 % humidity but on YSZ the capillary condensation at higher water pressures is pronounced. As the isothermal water uptake is evaluated on samples with an already existing ice-like layer, the zero point in Figure 5A is certainly not zero when the full amount of already pre-adsorbed H_2O molecules is taken into account. Since the evaluation of the FT-IR data at 3160 cm^{-1} provides this supplemental information, a comparison to estimate the offset of the dynamic moisture sorption measurements is provided in Figure 5B by plotting the FT-IR absorbance per m^2 on the left axis and the mol H_2O per m^2 on the right axis. With the knowledge that the lowest relative humidity in the dynamic moisture sorption experiment is 1%, this x-offset was set for the respective data. Additionally, an appropriate y-offset for the dynamic moisture sorption data was chosen for correlation with the FT-IR course after the bend. The obtained y-offset is $4.1 \cdot 10^{-5}$ mol m^{-2} for YSZ ($2.5 \cdot 10^{19}$ H_2O molecules m^{-2}, which would be additional 0.0104 % mass change) and $1.8 \cdot 10^{-5}$ mol m^{-2} for ZrO_2 ($1.1 \cdot 10^{19}$ H_2O molecules m^{-2},

additional 0.0015 % mass change). According to Raz et. al.[13] the area per molecularly adsorbed H_2O on YSZ is 10.8 Å^2 and the area per surface Zr center is at minimum 14.6 Å^2. Assuming that a hypothetical monolayer of molecularly adsorbed water on YSZ is "H-atom-interconnected" (promoted by the high amount of surface OH groups, leading to conduction in the EIS measurements, see also section 3.4), 10.8 Å^2 can be used as reference. On ZrO_2 the H_2O molecules are mainly bonded to the Zr-centers in a hypothetical monolayer of water (no conduction in the EIS data in section 3.4) and thus, 14.6 Å^2 should be taken as reference for the monolayer estimation. The water binding capacity of the ice-like water on YSZ is therefore roughly ~ 2.7 ML and for ZrO_2 ~ 1.6 ML. The further uptake of polymeric chained water up to 80 % relative humidity equals the amount of water in roughly ~ 2 additional ML for both oxides.

Comparing these findings to the generalized concept in section 3.1, these values again confirm the assumption that ZrO_2 is less hydroxylated than YSZ, which strongly lowers not only the amount of water in the ice-like layer, but also alters the binding mode. The higher amount of water in the ice-like layer on YSZ is clearly related to the higher amount of OH-groups/defects on the surface (increased polarity, better stabilization of the layer via hydrogen bonds to the surface) than for ZrO_2. The "few" OH-groups on ZrO_2 are, compared to YSZ, too far away of each other to sufficiently stabilize a total hydrogen-bonded wetting of the surface. In contrast, on YSZ a good stabilization of the OH-covered surface is likely for the ice-like layer and thus, the capacity of water uptake in this layer is increased relative to the un-doped oxide.

Since we assume that the ice-like layer is complete around the bend of the FT-IR plot in Figure 4 and Figure 5B, for every surface-normalized absorbance value a coverage with an associated pressure can be extracted from the data. Using the rough but usual approximation of a Langmuir model for this ice-like layer[13], a desorption enthalpy ΔH of ~56 kJ mol^{-1} for both oxides can be estimated. Furthermore, with this knowledge the temperature dependency

of the coverage within the ice-like layer on ZrO_2 and YSZ can be calculated: The coverage of the ice-like layer approaches zero around ~ 500 K at an equilibrium pressure of 24 mbar (see also Figure S4).

3.3. Electrochemical impedance spectroscopy

All impedance measurements are conducted in a flowing isobaric atmosphere of different partial pressures of water (He as carrier gas, flow ~ 1 mL s^{-1}). The samples are pre-treated in dry O_2 up to 1273 K, directly followed by the treatment in moist He without any contact to air. Thus, before water contact, the samples are assumed to provide comparable starting conditions (hydroxylated surface, no additional water layer) to the infrared experiments. Two distinct water partial pressures, 4 mbar and 24 mbar, were chosen. The starting point in the impedance spectra therefore represents the pre-treated sample that is exposed to a flowing water vapor/ helium stream leading to equilibrium water adsorption at the respective partial pressure. 4 mbar correspond to 17% relative humidity, which is comparable to the sorption data in Figure 4 at the beginning of the "plateau", representing polymeric chained/clustered water. 24 mbar correspond to almost 100% humidity near the saturation vapor pressure of water, i.e. near condensation, and thus, liquid-like water. Upon isobaric heating, more information about the contribution of water layers and hydroxylation to the impedance course can be obtained. For the most detailed comparison to the water experiments, Figure S5 provides correlating experiments in pure and dry He to distinguish the temperature-induced conduction contributions from the ones induced by H_2O/D_2O (t- and m-OH, ice-like water & polymeric chained water).

The study of Raz et al[13] provides a detailed theoretical background of the conductivity phenomenon of the different water layers on YSZ. Their perception of the layer model is basically consistent with the one stated in here. According to this study, the proton conduction in the chemisorbed water layer includes defect formation and proton hopping strongly associated with defects involving 'ZrO⁻' and 'ZrOH₂⁺' pairs. The conduction in the first

physisorbed water layer is dominated by H_3O^+ and OH^- and the proton conduction in a few physisorbed water layers is expressed by hydronium propagation $H_3O^+ + H_2O \rightarrow H_2O + H_3O^+$. There is a huge difference in the adsorption enthalpies of chemisorption (of the order of 100 kJmol^{-1}) and physisorption on top of the chemisorbed layers (a few kJmol^{-1} to tens of kJmol^{-1}) which is expressed by the fact that Raz et al. conclude that chemisorption plays a role up to a few hundred °C (chemisorbed layer is more than 50% complete below ~ 723 K and physisorption below T < 423 K). However, the above mentioned study provides investigations in at max. 3 mol% H_2O in O_2 or air up to max. 1073 K and it focusses exclusively on the pure conductivity contributions in/of the water layers. The present study is in good correlation with these results, but with the difference that we examine the whole oxide system in moist atmosphere up to a partial pressure of water near 1.

Additionally, Sato et al.[34] provide information about theoretical conduction mechanisms on hydrated ZrO_2 via proton migration on a cubic ZrO_2 (110) surface with hierarchically hydrogen-bonded H_2O layers and also chemisorbed species. Again the conductivity is directly mediated via "$ZrOH_2^+$" (acid sites) to "$Zr-OH^-$" (base sites) and connected to the surrounding chained H_2O molecules.

Before the discussion of the EIS experiments in H_2O and D_2O, a brief note about ultra-pure water (UPW) should be provided. It is already known from literature[35] that UPW has a conductivity of $\kappa = 0.05501$ μS cm^{-1} and hence, a resistivity of $\rho = 18.18$ MΩ cm at 298 K (cf. at 373 K: $\kappa = 0.7849$ μS cm^{-1}, $\rho = 1.274$ MΩ cm). However, these measurements are very sensitive to error sources (temperature ramps, used resistance temperature devices - introduction of gaseous or dissolved impurities during heating). With this knowledge one can assume that upon treatment of our samples in H_2O/D_2O also lower impedance values in the MΩ range in the low temperature region with liquid-like water "condensation" should be approached, if the surface is easily wetted (e.g. because of strong hydroxylation) and, thus, favors the formation of fully interconnected water layers.
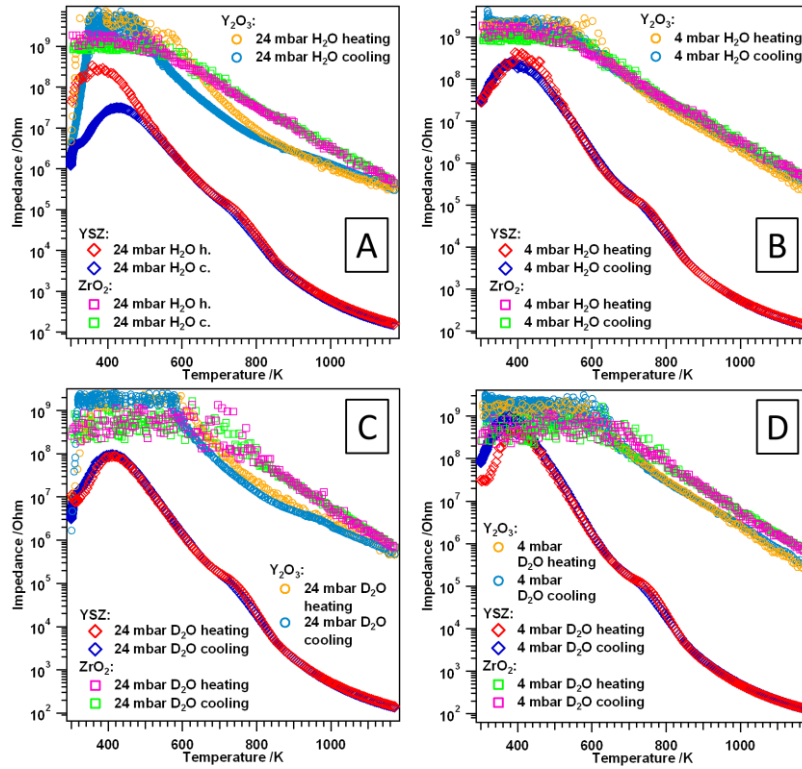
Figure 6: Temperature-dependent electrochemical impedance measurements on Y_2O_3, YSZ and ZrO_2 in flowing He (~ 1.0 mL s^{-1}) saturated with 24 and 4 mbar H_2O (panel A and B), 24 and 4 mbar D_2O (panel C and D). Linear heating and cooling rates of 10 K min^{-1} between RT and 1173 K were applied; "c" = cooling, "h" = heating.

Treatment in 4 and 24 mbar H_2O and D_2O

The electrochemical impedance measurements in Figure 6A-D (red and dark blue traces) show that water treatment of the YSZ sample in all four gas atmospheres (4 and 24 mbar either H_2O or D_2O) between room temperature (RT) and 1173 K leads to a similar trend during heating and cooling. An impedance value at RT of ~ $4 \cdot 10^7$ Ω, which is about 2 magnitudes lower than under dry conditions, is obtained at the beginning of the heating routine. Upon heating between RT – 410 K the impedance is rising, which is due to the removal of the physisorbed water multilayers contributing to a higher conductivity. This is also exactly the beginning of the first Arrhenius-fitted temperature region for the heating and cooling procedures (408 – 515 K; depending on the used gas treatment and pressure) in the

25

corresponding Arrhenius plot (Figure 7C and Table S2). Starting at T > 410 K the impedance starts to drop, exhibiting semiconductive behavior (final value of ∼ $1 \cdot 10^2$ Ω at 1173 K). During re-cooling, almost the exact same impedance course is apparent, and in 4 mbar H_2O and D_2O final values in the 10^7 Ω range are again attained at RT. On the YSZ samples treated in 24 mbar H_2O/D_2O the impedance drops to even lower values in the 10^6 Ω range. Another general characteristic feature is visible in the temperature-dependent impedance spectra of YSZ in the area between 673 K – 873 K as a "bump" at ∼ 750 K (note that this is exactly the temperature where two different temperature regimes with different E_A's are present in the Arrhenius plot in Figure 7 and Table S2). It is already known from comparable studies[18, 19] that different areas in the whole temperature-range can be defined, where changes of charge transfer mechanisms, e.g. at grain boundaries, contribute to the total impedance/conductivity: in the additional He experiment in Figure S5, up to ∼ 750 K the impedance is strongly influenced by hydroxyl-mediated charge-transfer at the grain boundaries, and starting at T > 750 K pure oxide ion transfer is most likely becoming dominant due to progressive surface dehydroxylation.
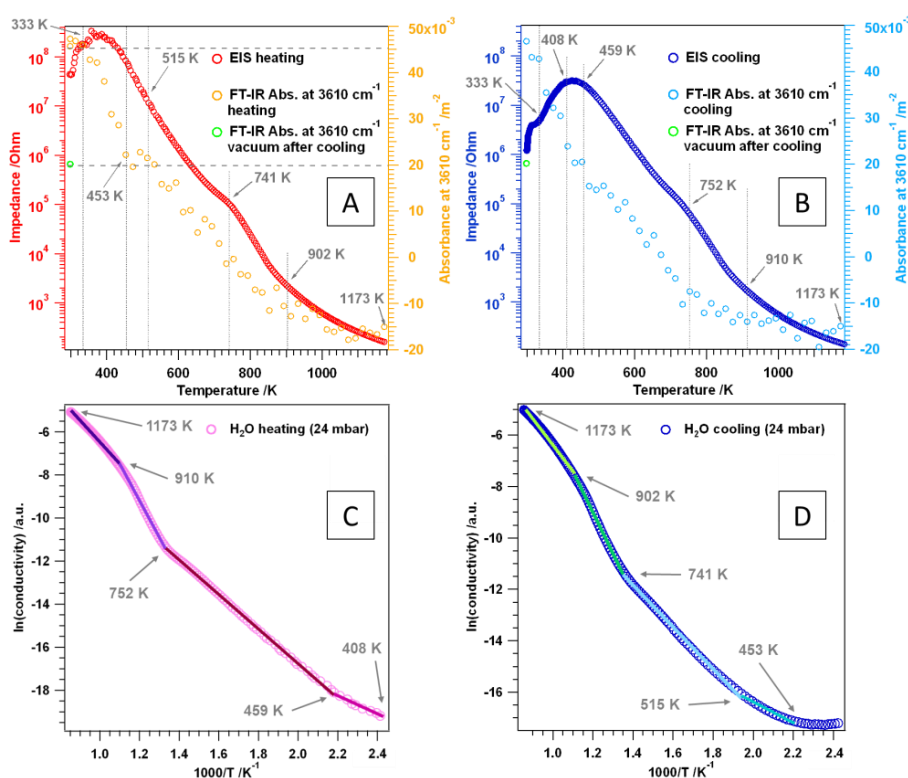

26

Figure 7: Correlation of EIS and FT-IR data on YSZ in 24 mbar H_2O (flow ~1 mL s^{-1}, He carrier gas). Comparison of the electrochemical impedance with the relative FT-IR absorbance at 3160 cm^{-1} upon (A) heating and (B) cooling. Corresponding Arrhenius plots of (C) heating and (D) cooling electrochemical impedance traces in 24 mbar H_2O.

The exactly same experiment on YSZ in 24 mbar H_2O was also performed in the FT-IR setup, monitoring especially the broad water feature at the characteristic wavenumber of 3160 cm^{-1}. Upon plotting the absorbance of the IR signal at 3160 cm^{-1} and the impedance signal over the whole temperature range (Figure 7A and B, see also Figure S6), and comparing the qualitative course of both traces to the respective to Arrhenius fits (cf. Figure 7C and D and Table S2), the varying influence of physisorbed and chemisorbed water can be, at least qualitatively, extracted. Between RT and 333 K the infrared signal at 3160 cm^{-1} in Figure 7A stays constant even though there is an increase of almost 1 magnitude in the impedance signal. This confirms that the chosen wavenumber is not absolutely representative for all adsorbed water molecules. In fact, FT-IR is insensitive with respect to liquid-like water layers/molecules that are very far away from the surface where diffusional mobility/dynamic change of dipolar orientation of the whole water molecules becomes more likely. This is exactly the reason for the insensitivity of IR toward "liquid-like" condensed water in the measurements at p/p_0 values close to 1, in comparison to the rather drastic increase in the sorption measurements in Figure 4B, which verify the expected condensation.

The first impedance rise (up to ~350 K) corresponds to the removal of water layers which are obviously IR-invisible (flat region in the absorbance plot) and exhibit a negative apparent activation energy with respect to charge carrier concentration (not plotted in Figure 7C). These "liquid" layers provide a pronounced conductivity-enhancing contribution (roughly corresponding to the conductivity of pure water[35]), contributing - along with the associated loss of conducting polymeric chained and ice-like species - to the strong resistivity increase

upon removal, until the maximum position around 380 K is reached. Further heating leads to a fast decrease of the impedance, which nevertheless stays clearly below the values in dry He, due to the presence of both molecularly and dissociatively adsorbed water. The IR absorbance shows no such maximum, but a continuous and pronounced decrease of absorbance between ~350 and ~ 450 K. This means that above 350 K the "IR-visible", i.e. already rather surface-near water species are desorbing, in the order polymeric-chained water, followed by ice-like water. This region corresponds to p/p_0 values between < 0.6 (water partial pressures < 15 mbar) in the adsorption isotherm of YSZ in Figure 3. As has been shown (Figure S5, equilibrium calculations in 3.3), temperatures around 450 K at 24 mbar equilibrium pressure are sufficient to deplete even the more strongly bonded ice-like layer (remaining after more or less complete desorption of the polymeric chain water) to ~13% of its hypothetical Langmuir saturation value.

Further heating above 450 K leads to a less steep decrease in the infrared absorbance up to ~ 900 K that is most likely associated with the further removal of remaining strongly bonded water molecules along with chemisorbed OH species. Above this temperature, the "negative" absorbance changes in the "broad feature" region (interconnected dense OH layer) are assigned to further dehydroxylation, i.e. depletion of chemisorbed water species (see also Figure S6). Re-cooling (Figure 7B) shows a similar trend: no OH-signal increase is observed until ~ 900 K, followed by a continuous re-hydroxylation/ dissociative water uptake upon further cooling to ~ 500 K. Subsequently, a faster increase in the course of the infrared signal is again observed in the region where the impedance exhibits a maximum (~ $3 \cdot 10^7$ Ω) and drops again due to cumulative molecular water adsorption below ~ 450 K. At 333 K the impedance shows a small plateau (~ $4 \cdot 10^6$ Ω, with a similar value in 24 mbar D_2O, Figure 6C), corresponding to an one magnitude lower impedance value in comparison to the 333 K point during heating. This plateau correlates with a step-like increase in the intensity of the IR signal as compared to the heating trace, suggesting even stronger hydroxylation during

cooling and thus, an increased water capacity in the physisorbed layers (see also green "vacuum" reference data point in Figure 7B). Further cooling leads to a continuous decrease of the impedance to $\sim 1 \cdot 10^6$ Ω at an almost constant infrared signal. The vacuum FT-IR spectrum after this heating and cooling routine reveals an increased amount of chemisorbed m-OH groups at 3704 cm^{-1} (see also Figure S6). This is correlated with the smaller impedance value after cooling (in comparison to the start of the experiment) and is also reflected by a Nyquist plot with two semicircles (see detailed discussion below). Since the impedance experiments in 4 mbar H_2O and D_2O correspond to 17% humidity (beginning of the "polymeric chained water plateau" in the sorption measurement of Figure 4 with no liquid-like water layers) the plateau at 24 mbar/ 333 K is not observed and the impedance after the whole heating/cooling cycle is very similar to the value at the beginning ($\sim 3 \cdot 10^7$ Ω, see Figure 6C and D). Table 2 gives an overview of the micro/macroscopic layer-by-layer model on which the interpretation/ quantification of the results is based. The impact of the four distinct adsorption categories of H_2O on YSZ to the respective measurement techniques is summarized.

Table 2. Comparison of the impact of the distinct water adsorption models to the isothermal and isobaric FT-IR, sorption and EIS measurements on YSZ.

YSZ	FT-IR signal at 3160 cm^{-1}	sorption measurement	EIS
liquid-like water layers	*impact on the signal at isothermal conditions:* no effect on IR signal *removal/uptake isobaric conditions:* T < 333 K	strong increase above 80 % relative humidity	*removal/uptake isobaric conditions:* RT – 333 K 24 mbar H_2O/D_2O: impedance at RT $\sim 1 \cdot 10^6$ Ω
polymeric chained water molecules	*impact on the signal at isothermal conditions (RT):* p > 1 mbar *removal/uptake isobaric conditions:* 333 K < T < 500 K	region between 1% and 80 % relative humidity	removal/uptake isobaric conditions: 333 – 380 K 24 mbar H_2O/D_2O: impedance at RT $\sim 3 \cdot 10^7$ Ω
ice-like water layers	*impact on the signal at isothermal conditions(RT):* p < 1 mbar	<1% relative humidity, starting conditions of moisture sorption	*removal/uptake isobaric conditions:* 380 - 500 K

	removal/uptake isobaric conditions: 333 K < T < 500 K	measurement	
reversible chemisorption/ OH groups	*impact on the signal at isothermal conditions:* p < 10^{-3} mbar *removal/uptake isobaric conditions:* 500 K < T < 900 K	-	*Removal/uptake isobaric conditions:* 500 – 900 K increased amount after re-cooling → decreased impedance value, Nyquist plot after re-cooling via enhanced protonic conduction

The temperature-related conduction mechanisms of the YSZ pellet in moist atmosphere can be summarized as follows: up to ~ 450 K decreasing impact of the proton conduction and up to 750 K hydroxyl-mediated oxide-ion transfer at the grain boundaries with a stable OH density on the surface. Above 750 K a transient zone with progressive dehydroxylation is suggested, where hydroxyl-mediated and pure O^{2-} conduction at grain boundaries is present and at even higher temperature, only the pure O^{2-} conduction is dominant in the bulk as well as at the grain boundaries. This is also in good agreement with a study conducted by Scherrer et al. [36] who also postulated these three temperature regions with different conduction mechanisms that can be distinguished on YSZ.

For direct comparison to YSZ, Figures 6A-D (pink and light green traces) show the corresponding impedance measurements on ZrO_2. Only two distinct temperature regions are visible in all four measurements: the first one is between RT and ~ 600 K in H_2O (RT and ~700 K in D_2O) and the second one at T > 600 K for treatment in H_2O and T > 700 K for D_2O. The first temperature region is a plateau-like region in the GΩ range (detection limit of EIS spectrometer) where the sample shows perfectly insulating properties, and in the second one the sample exhibits semiconductive properties (final value of ~ $5 \cdot 10^5$ Ω at 1173 K on all four samples). Upon re-cooling, exactly the same trend as for the heating routine is apparent and there are hardly any differences in the impedance course. In all four gas atmospheres and partial pressures there is no decreased impedance between RT and 350 K on ZrO_2, as seen on

the other oxides. Thus, the equivalent layers of physisorbed water (with respect to ice-like/polymeric chained layer capacity) on this oxide – matching the findings of FT-IR and sorption measurements – do not contribute to the overall impedance/conductivity of the sample at all. As derived from the discussion of Figure 5 in section 3.3, the almost doubled amount of adsorbed water on YSZ in the complete ice-like state (prior to the sorption of polymeric chained water) can be in part assigned to the substantial coverage with dissociated/chemisorbed water species. In essence, the predominantly molecular/physisorbed ice-like water layer and also the following layers on the strongly and irreversibly de-hydroxylated pure monoclinic ZrO_2 exhibit no measurable protonic conductivity. This result is consistent with the absence of the proton hopping mechanism proposed by Raz et al.[13] for YSZ, which is inherently linked to the presence of a sufficient density of hydroxyl groups on ZrO_2 from water dissociation. In this view, the absence of protonic conduction can be regarded as a clear proof for the inability of high-temperature annealed monoclinic ZrO_2 surfaces to dissociate a relevant amount of water in the whole experimental temperature range. Obviously, both conduction mechanisms proposed by Raz[13] for the chemisorbed and the following ice-like layer are inhibited. Furthermore, the additional polymeric-chained and liquid-like water species are equally insulating up to water condensation at ~24 mbar. This, moreover, suggests the absence of a fully percolated water film between the grains only on ZrO_2. All these results set pure monoclinic ZrO_2 very much apart from the more surface-reactive YSZ and Y_2O_3.[16] Figure S7 shows the comparison of the temperature dependent evaluation of the FT-IR data of YSZ and ZrO_2 in 24 mbar H_2O at 3160 cm^{-1}. As already mentioned, this wavenumber represents a binding state of water molecules or OH groups that are interconnected. Due to the high amount of OH-groups on YSZ also the chemisorbed OH species do contribute to this signal (saved in the background and thus, "negative" values are possible for YSZ). In contrast, on ZrO_2 the few chemisorbed OH species are far away of each other and do not contribute to this signal and are not evaluated in this plot. In fact, in Figure S7 for ZrO_2 the pure

contribution of polymeric chained and ice-like water is displayed, which is perfectly correlated with the model calculation in Figure S4.

When exposing the (most easily and deeply hydrolysable) Y_2O_3 sample to 24 mbar H_2O and D_2O and restricting the heating up to around 1173 K (Figure 6A and C yellow and light blue traces) basically three temperature regions in the temperature-dependent impedance spectra can be distinguished: the first one between RT and ~ 350 K where the liquid-like water layers contribute strongly, the second from 350 K up to ~ 600 K with a plateau-like impedance behavior, and the third one at T > 600 K, exhibiting semiconductive behavior. At the maximum temperature an impedance value of ~ $3 \cdot 10^5$ Ω at 1173 K is obtained (note that the value for YSZ at this temperature is 3 magnitudes lower due to its high oxide ion conductivity). In Figure 6A differences in the heating and cooling procedures are apparent between 508 – 906 K. This discrepancy is due to the fact that during the heating and cooling routine even more OH-groups are generated – i.e. the proceeding hydrolysis of the Y_2O_3 surface near regions leads to a gradually improved conductivity. Upon re-cooling to RT a very similar trend as in the beginning of the experiment is observed: the impedance starts to decrease again due to physisorbed water layers with a final value of $4 \cdot 10^6$ Ω at RT. This is comparable to the value obtained for the plateau at ~ 333 K for YSZ with ~ $1 \cdot 10^6$ Ω. Upon treatment of Y_2O_3 in 24 mbar D_2O (Figure 6C), again, differences in the heating and cooling procedures are apparent between 573 – 973 K, but they are not as pronounced as during treatment in 24 mbar H_2O. Upon re-cooling at 573 K the impedance is in the GΩ area, until at T < 330 K it starts to decrease again leading to a value of ~ $2 \cdot 10^6$ Ω at RT. The fact that the condensed water film exhibits conductivity values close to those of pure water[35] indicates that full percolation of this film is attained, most likely because of more efficient, hydroxylation-induced surface wetting, in strong contrast to pure ZrO_2. Vice versa, the ice-like and polymeric chained water layers on Y_2O_3 are equally insulating as on ZrO_2, meaning that the above-discussed proton hopping mechanism is absent. A possible explanation comes from the

high basicity of Y_2O_3 (rather associated with OH^- anionic species) as compared to YSZ, where comparably acidic Zr-OH entities are present.

If the Y_2O_3 samples that are treated in 4 mbar H_2O and D_2O (Figure 6B and D yellow and light blue traces) are compared to each other, an almost identical impedance course is observed for the heating and cooling curves. No measurable impact of proton conduction in physisorbed water layers below the condensation limit occurs (like it was the case for 24 mbar). This shows again that only a fully percolated water film with its intrinsic conductivity can explain the high RT/ 24 mbar conductivity on Y_2O_3.

To sum up, pronounced differences between the three samples, being strongly dependent on the different gas treatments and partial pressures, wre observed. In general, YSZ shows the highest conductivity (lowest impedance) which is due to its high oxide ion conduction at high temperatures. Y_2O_3 and ZrO_2 show impedance values that are about three magnitudes higher than the ones obtained for YSZ at 1173 K. Depending on the H_2O/D_2O partial pressure (24 or 4 mbar) and the sample a lower impedance in the temperature range between RT − 355 K (Y_2O_3: 24 mbar H_2O and D_2O) and RT − 410 K (YSZ: 4 and 24 mbar H_2O and D_2O) in comparison to dry conditions (Figure 6) is obtained, which is due to the formation and removal of physisorbed water layers.
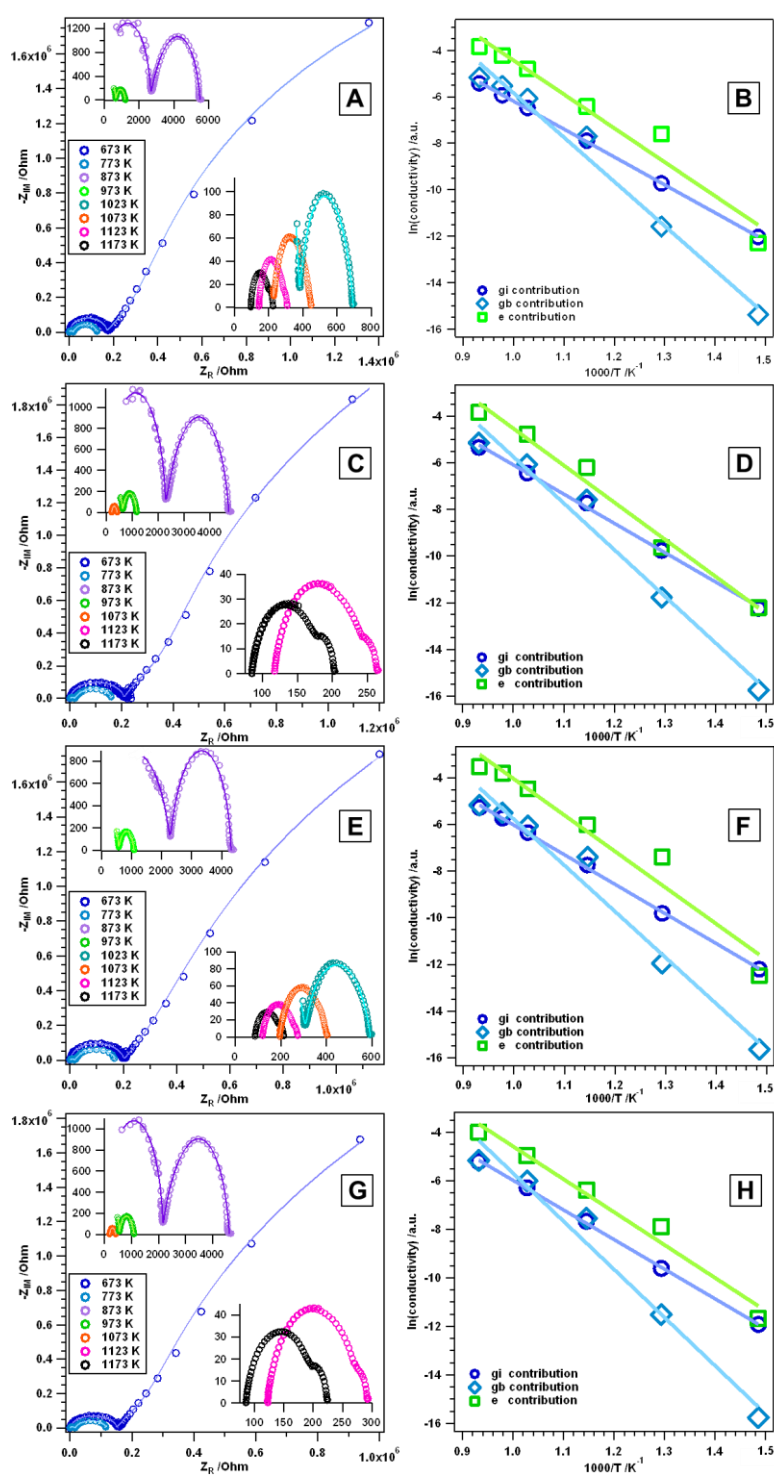
Figure 8: Nyquist plots (data points), simulated spectra (continuous lines) and Arrhenius plots of the grain interior, grain boundary and the electrode contribution of a YSZ powder pellet sample treated in 24 mbar H_2O (panel A and B), 4 mbar H_2O (panel C and D), 24 mbar D_2O (panel E and F) and 4 mbar D_2O (panel G and H) (flow ~ 1.0 mL s^{-1}) at selected

temperatures between RT and 1173 K. The lowest frequency of 0.1 Hz is at the right side and the highest one of 0.1 MHz at the left side of the x-axis in the NP's. The insets in panels A, C, E and G show zoomed regions of the NPs at higher temperatures.

Figure 8 highlights the corresponding Nyquist plots (NP's) of the YSZ sample treated in different gas pressures (4 and 24 mbar) of H_2O and D_2O in flowing He at different temperatures. At 673 K, a frequency-dependent impedance plot with two "semicircles" is apparent with a small one at high frequencies (HF) and a very big one at low frequencies (LF). Note that in the chosen frequency range of 0.1 Hz − 0.1 MHz this low frequency semicircle is not completely pictured in the frequency dependent impedance spectra. At T ≥ 773 K two well-defined semicircles are visible: a very large one at high frequencies (HF) and a smaller one at low frequencies (LF) with "tailing". If the system is heated up to 873 K a different trend becomes apparent: the maximum of the two arcs and, hence, the resistance of these two processes is very similar. It is already known from literature[18, 19], that in this temperature region the surface conductivity phenomena become increasingly dominated by bulk ion conductivity. The higher the temperature gets, the less influence surface chemistry has on the conductivity and hence, on the frequency dependent impedance experiments.

At temperatures of 923 K and beyond, the relative resistivity contributions of the two arcs change again, resulting in a dominant first arc at high frequencies. If the system is heated up to even higher temperatures (see insets in the upper right corner, Figure 8A, C, E, G), another trend becomes clear: starting at T ≥ 873 K, the HF semicircle of the NP is getting less and less pronounced in the chosen frequency range, which also makes it difficult to exactly determine the maximum intensity of this contribution with respect to the resistance and capacitance. At a temperature of 1073 K only a few data points of the first semicircle are present and at 1123 K basically no contribution of the first semicircle is visible (note that this does not indicate that this contribution is not present anymore − as mentioned before it is simply not detectable

within the chosen frequency range). Due to the lack of data points for the HF Nyquist plot at 1123 K and 1173 K, no fit could be applied. As shown in Figure 8A and E, basically the same trends apply to the different measurements, although conducted in different gas atmospheres.

A general trend for all gas treatments in Figure 8 can be observed: both the HF and LF contributions (this will be later related to grain interior gi and gb contribution) significantly decrease during the measurement whilst heating the system to higher temperatures. Thus, the higher the temperature, the lower the contribution of these parameters is. The numerical values of the respective capacitive and resistive parameters at the chosen temperatures are also shown in Table S3 – S6.

Many attempts have been made to find the most representative, but at the same time also most simple, equivalent circuit model for a powder-based ionic conductor such as YSZ.[37-54] However, this is not an easy task, because - in contrast to single crystal YSZ samples - additional parameters have to be taken into account, in particular grain size and grain boundary effects.[39, 40, 48, 49, 52, 55, 56] As the semicircles are often a complex superposition of the distinct involved processes, the complete and unambiguous disentanglement of the resistivity and capacitance contributions becomes difficult.[47, 49] Nevertheless, sufficiently reliable fit models (originally by Bäuerle et al.[26]) have already been established and their validity proven.[19, 38] From a previous study[19] and literature data,[49, 54] it is already known that the grain interior (bulk) contribution is usually observed at high frequencies, whereas grain boundary and electrode contributions are located at mid and lower frequency part of the Nyquist plot, respectively. The "tailing" of the arc in the low frequency range is due to interaction between the electrode and the sample pellet.[19, 49, 54] This described "tailing" is actually the onset of another semicircle which is, as mentioned before, due to electrode interface contribution and is usually more pronounced at higher temperature.

The circuit that we used in this study to fit the experimental data is composed of constant phase elements (CPE's) instead of ideal (Debye) capacitors (Figure 9). This is common for

polycrystalline samples due to material inhomogeneity, surface defects such as pores, electrode roughness and ionic transport deviation from Fick's law, giving rise to a certain degree of frequency dispersion and non-uniformity of the current density. Hence, these elements more accurately represent the capacitive behavior of this kind of cell in the whole studied frequency range (which can also be clearly seen in the depressed semicircles).[53, 57, 58]

Using the equivalent circuit model, the capacitances (C) were calculated using the formula

$$C = (R^{1-\alpha} \cdot Q)^{1/\alpha} \qquad [1]$$

with Q being the value obtained for the respective CPE and α indicating whether the CPE behaves more like an ideal capacitor (α = 1) or more like an ideal resistance (α = 0).

The parameters of the equivalent circuit model used to fit the experimental data are summarized in Tables S3 – S6. The basic agreement of the simulated spectra with the experimental data supports the general validity of the equivalent circuit diagram and also the comparison to other studies on similar materials and under comparable conditions. The comparison of the experimental values for the different contributions to other works in literature on the same or similar materials and conditions also supports this.[40, 41, 45, 49, 51, 53, 55, 59-65]
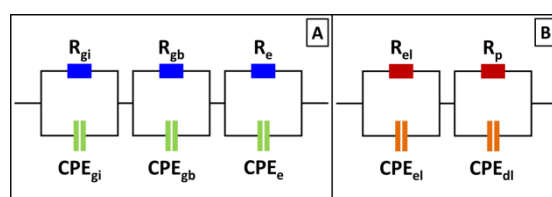

Figure 9: Equivalent circuit model used for fitting the frequency-dependent impedance data of the samples represented in Figure 9 (A) between 673 – 1073 K with contributions from the grain interiors (gi), grain boundaries (gb) and electrode (e) without liquid-like water film; (B) fit model for the NP's during treatment in 24 mbar H_2O/D_2O after re-cooling to RT with contributions from the electrolyte (el) and chemical polarization (p) of the electrode and double layer (dl) with fully percolated liquid-like water film (for the discussion of Figure S9).

With the equivalent circuit (Figure 9A) it is now possible to distinguish the different contributions for the different processes (gi, gb and e). With this information, the temperature dependency of these contributions in the different gas atmospheres and under different partial pressures could be elucidated (Tables S3 – S6). One of the trends that all measurements have in common is that the higher the temperature, the lower the impedance contributions are, converging to a final value. At the lower temperatures (673 and 773 K) the grain boundary contribution is for all experiments one magnitude lower than the one from the grain interiors. Starting at T > 773 K this ratio changes and the contributions are comparable. At least with respect to the impedance behavior without extended liquid-like water layers, there are basically only small differences between the different moist gas treatments at 4 and 24 mbar H_2O/D_2O.

If the values in Table S3 – S6 are compared to the ones found in literature, again differences/similarities can be outlined. Similar C_{gi} values as ours have been found by e.g. Lacroix et al. $(SrZr_{0.9}Ln_{0.1}O_{2.95})$.[45] For the grain boundary capacitance, 8-ScSZ[66] shows a similar clear trend: the higher the temperature (maximum 723 K) the higher the value for the grain boundary capacitance. A C_{gb} value of $1.71 \cdot 10^{-6}$ F at 723 K was reported. Verkerk et al.[48] also studied the impact of grain size on the C_{gb}. He found a value of ~ $3.0 \cdot 10^{-6}$ F at 673 K for an alkoxide sample $[(ZrO_2)_{1-x} (YO_{1.5})_x; x = 0.164]$ with a grain size of ~ 13μm and also ~ $3.0 \cdot 10^{-6}$ F at 673 K for a Zircar sample $[(ZrO_2)_{1-x} (YO_{1.5})_x; x = 0.140]$ with a grain size of ~ 11μm. It has already been stated in literature[54] that there are two temperature regimes for a Pt│YSZ│Pt cell such as the one that we used: a low temperature region up to 720 K where the Pt electrode behaves as blocked and the capacitance assumes values between $10^{-12} – 10^{-10}$ F (note that grain boundary capacitance values of Nyquist plots at the lowest temperature of 673 K fit quite well with this) and a high temperature region (T > 720 K) with capacitances up to 10^{-3} F. The grain boundary capacitance values of the Nyquist plot at 673 K for all 4 different gas treatments and pressures fits very well with the values in the low temperature

region. However, the ones that we obtained at T > 720 K are much lower than the ones stated by Wierzbicka et al.[54] (discrepancies of ~ 3/4 magnitudes).

Using the obtained resistance values for R_{gi}, R_{gb} and R_e, an Arrhenius plot of ln(conductivity) of the respective contribution vs. the reciprocal of the temperature in the temperature region between 673 – 1073 K (Figure 8B, D, F, H) yields the "apparent" activation energies for the different contributions. For detailed numerical values see Table S7. An average value of ~ 1,06 eV (110 kJmol^{-1}) for all 4 gas treatments is obtained for the grain interior process, perfectly fitting to the activation energy for bulk anion conductivity in YSZ.[38] In contrast, the highest activation energy value of ~ 1.69 eV (175 kJmol^{-1}) of all three processes is obtained for the grain boundary contribution. In general, the values for $E_A(gi)$ and $E_A(gb)$ show a very similar temperature trend and are hardly distinguishable with respect to the water pressure. In contrast to this result, the activation energies for the electrode process differ to some extent, depending on the used H_2O/D_2O treatment/partial pressure (Tables S3 – S6). If the obtained values for $E_A(gi)$ and $E_A(gb)$ in this work are compared with the ones found in literature,[36, 38, 42, 52-54, 56, 60, 63, 65, 67, 68] some of the experimental data agree quite well with the values from this work - especially the values obtained for $E_A(gi)$. Concerning the activation energy for the grain boundaries, different E_A's can be extracted from literature, most of them being lower than the values that we calculated. However, there are some reports of higher activation energies for this process that are very similar to ours, especially the one that Gong et. al.[65] obtained. These differences in the obtained E_A's can be easily explained in terms of different pre-treatments of the samples, gas atmospheres and different experimental conditions e.g. moist or dry conditions, different heating rates, different temperature regions used for the linear fits. However, comparable values for $E_A(e)$ could not be found due to the lack of literature data.

4. Conclusions

The combined study of water adsorption on the ceramic oxides YSZ, ZrO_2 and Y_2O_3 using *operando* FT-IR spectroscopy, *operando* electrochemical impedance spectroscopy and dynamic moisture sorption measurements allowed to experimentally verify a pressure- and temperature-dependent layer-by-layer adsorption model with clearly distinguishable states of (1) chemisorbed OH groups at low pressures and high temperatures, acting as "anchors" as well as proton-donors for the gradually more and more weakly bonded (2) ice-like, (3) polymeric chained and (4) liquid-like molecular water layers. The absence of the reversibly populated chemisorbed water species on pure monoclinic ZrO_2 could be verified and directly related to the absent protonic conductivity of the respective water films. Concerning the distinct adsorption energetics, binding strengths and conduction properties observed with increasing water coverages, well-correlated data in the pressure range from 10^{-5} mbar up to ambient pressure and the temperature range between 1173 K and RT were obtained, bridging the gap between low-temperature (U)HV and high-temperature ambient pressure investigations. It was possible to assign basically all discrete signals/regions in the infrared spectra to the different water binding states. From the related EIS investigations on YSZ, the temperature- and pressure-related stability and protonic conductivity of the water layers/ adsorbed states could be quantified. Independently from the low-temperature water surface chemistry, activation energies and the anionic resistivity contributions of grain interior, grain boundary and the electrode could be quantified in the presence of water vapor up to 1173 K. A perfect correlation of the temperature dependent impedance course and the related water adsorption stages with the infrared data obtained under identical experimental conditions clarifies the impact of water/OH-groups on YSZ at close to SOFC relevant conditions (temperatures up to 1173 K, ambient pressure). The specific impact of water on the YSZ-based anode- and electrolyte surfaces and -interfaces can, thus, be considered as a basis of further application-oriented investigations of the oxides in other gases mixed with water

vapor, since under realistic high-pressure and high-temperature conditions of relevant fuel gas and/or reforming mixtures a certain amount of dissociated water and dynamic surface hydroxylation is most likely always present.

Finally, with regard to low-temperature catalytic reforming processes occurring already around 500 K (e.g. methanol steam reforming), the relative population and the specific reactivities of the ice-like molecular and dissociated water species could be provided in order to correctly assess the potential co-catalytic function of ZrO_2-based oxidic support materials for efficient water activation. In this view, it appears highly interesting to study the consequences of the strongly different water chemisorption properties of e.g. YSZ and pure ZrO_2 polymorphs with respect to reforming activity and selectivity.

5. Acknowledgments

Supporting Information provides additional FT-IR experiments and impedance measurements, as well as additional Tables with parameters of the impedance peak fitting routines.

References

(1) Schlögl, R., Heterogeneous Catalysis. *Angew. Chem. Int. Edit.* **2015,** *54* (11), 3465-3520.

(2) Daniells, S. T.; Overweg, A. R.; Makkee, M.; Moulijn, J. A., The Mechanism of Low-Temperature CO Oxidation with Au/Fe_2O_3 Catalysts: A Combined Mössbauer, FT-IR, and TAP Reactor Study. *J. Catal.* **2005,** *230* (1), 52-65.

(3)   Zhang, Z.; Du, Y.; Petrik, N. G.; Kimmel, G. A.; Lyubinetsky, I.; Dohnalek, Z., Water as a Catalyst: Imaging Reactions of O_2 with Partially and Fully Hydroxylated TiO_2(110) Surfaces. *J. Phys. Chem. C* **2009,** *113* (5), 1908-1916.

(4)   Moreau, F.; Bond, G. C.; van der Linden, B.; Silberova, B. A. A.; Makkee, M., Gold Supported on Mixed Oxides for the Oxidation of Carbon Monoxide. *Appl. Catal. A* **2008,** *347* (2), 208-215.

(5)   Leist, U.; Ranke, W.; Al-Shamery, K., Water Adsorption and Growth of Ice on Epitaxial Fe_3O_4(111), FeO(111) and Fe_2O_3(biphase). *Phys. Chem. Chem. Phys.* **2003,** *5* (11), 2435-2441.

(6)   Henderson, M. A., The Interaction of Water with Solid Surfaces: Fundamental Aspects Revisited. *Surf. Sci. Rep.* **2002,** *46* (1-8), 1-308.

(7)   Smith, R. J. B.; Loganathan, M.; Shantha, M. S., A Review of the Water Gas Shift Reaction Kinetics. *Int. J. Chem. Reac. Eng.* **2010,** *8*, 34.

(8)   Caporali, R.; Chansai, S.; Burch, R.; Delgado, J. J.; Goguet, A.; Hardacre, C.; Mantarosie, L.; Thompsett, D., Critical Role of Water in the Direct Oxidation of CO and Hydrocarbons in Diesel Exhaust After Treatment Catalysis. *Appl. Catal. B* **2014,** *147*, 764-769.

(9)   Royer, S.; Duprez, D., Catalytic Oxidation of Carbon Monoxide over Transition Metal Oxides. *ChemCatChem* **2011,** *3* (1), 24-65.

(10)   Li, S. Y.; Jia, M. J.; Gao, J.; Wu, P.; Yang, M. L.; Huang, S. H.; Dou, X. W.; Yang, Y.; Zhang, W. X., Infrared Studies of the Promoting Role of Water on the Reactivity of Pt/FeOx Catalyst in Low-Temperature Oxidation of Carbon Monoxide. *J. Phys. Chem. C* **2015,** *119* (5), 2483-2490.

(11)   Sa, S.; Silva, H.; Brandao, L.; Sousa, J. M.; Mendes, A., Catalysts for Methanol Steam Reforming-A Review. *Appl. Catal. B* **2010,** *99* (1-2), 43-57.

(12) Achenbach, E.; Riensche, E., Methane Steam Reforming Kinetics for Solid Oxide Fuel Cells. *J. Power Sources* **1994,** *52* (2), 283-288.

(13) Raz, S.; Sasaki, K.; Maier, J.; Riess, I., Characterization of Adsorbed Water Layers on Y_2O_3-doped ZrO_2. *Solid State Ionics* **2001,** *143* (2), 181-204.

(14) Kogler, M.; Köck, E. M.; Bielz, T.; Pfaller, K.; Klötzer, B.; Schmidmair, D.; Perfler, L.; Penner, S., Hydrogen Surface Reactions and Adsorption Studied on Y_2O_3, YSZ, and ZrO_2. *J. Phys. Chem. C* **2014,** *118* (16), 8435-8444.

(15) Mukhopadhyay, M.; Mukhopadhyay, J.; Basu, R. N., Functional Anode Materials for Solid Oxide Fuel Cell - A Review. *T. Indian Ceram. Soc.* **2013,** *72* (3), 145-168.

(16) Köck, E. M.; Kogler, M.; Bielz, T.; Klötzer, B.; Penner, S., In Situ FT-IR Spectroscopic Study of CO_2 and CO Adsorption on Y_2O_3, ZrO_2, and Yttria-Stabilized ZrO_2. *J. Phys. Chem. C* **2013,** *117* (34), 17666-17673.

(17) Kogler, M.; Köck, E. M.; Perfler, L.; Bielz, T.; Stöger-Pollach, M.; Hetaba, W.; Willinger, M.; Huang, X.; Schuster, M.; Klötzer, B.; Penner, S., Methane Decomposition and Carbon Growth on Y_2O_3, ZrO_2, and Yttria-Stabilized ZrO_2. *Chem. Mater.* **2014,** *26* (4), 1690-1701.

(18) Kogler, M.; Köck, E. M.; Klötzer, B.; Schachinger, T.; Wallisch, W.; Henn, R.; Huck, C. W.; Hejny, C.; Penner, S., High-Temperature Carbon Deposition on Oxide Surfaces by CO Disproportionation. *J. Phys. Chem. C* **2016,** *120* (3), 1795-1807.

(19) Kogler, M.; Köck, E.-M.; Klötzer, B.; Perfler, L.; Simon, P., Surface Reactivity of YSZ, Y_2O_3, and ZrO_2 toward CO, CO_2, and CH_4: A Comparative Discussion. *J. Phys. Chem. C* **2016,** *120* (7), 3882–3898.

(20) Köck, E.-M.; Kogler, M.; Pramsoler, R.; Klötzer, B.; Penner, S., A High-Temperature , Ambient-Pressure Ultra-Dry Operando Reactor Cell for Fourier-Transform Infrared Spectroscopy. *Rev. Sci. Instrum.* **2014,** *85* (8), 084102.

(21) Wagner, W.; Riethmann, T.; Feistel, R.; Harvey, A. H., New Equations for the Sublimation Pressure and Melting Pressure of H_2O Ice Ih. *J. Phys. Chem. Ref. Data* **2011,** *40* (4), 11.

(22) Thiel, P. A.; Madey, T. E., The Interaction of Water With Solid Surfaces – Fundamental Aspects. *Surf. Sci. Rep.* **1987,** *7* (6-8), 211-385.

(23) Kouva, S.; Honkala, K.; Lefferts, L.; Kanervo, J., Review: Monoclinic Zirconia, its Surface Sites and Their Interaction With Carbon Monoxide. *Catal. Sci.Technol.* **2015,** *5* (7), 3473-3490.

(24) Takeuchi, M.; Martra, G.; Coluccia, S.; Anpo, M., Investigations of the Structure of H_2O Clusters Adsorbed on TiO_2 Surfaces by Near-Infrared Absorption Spectroscopy. *J. Phys. Chem. B* **2005,** *109* (15), 7387-7391.

(25) He, M. Y.; Ekerdt, J. G., Infrared Studies of the Adsorption of Synthesis Gas on Zirconium Dioxide. *J. Catal.* **1984,** *87* (2), 381-388.

(26) Bianchi, D.; Gass, J. L.; Khalfallah, M.; Teichner, S. J., Intermediate Species on Zirconia Supported Methanol Aerogel Catalysts. 1. State of the Catalyst Surface before and after the Adsorption of Hydrogen. *Appl. Catal. A* **1993,** *101* (2), 297-315.

(27) Bachiller-Baeza, B.; Rodriguez-Ramos, I.; Guerrero-Ruiz, A., Interaction of Carbon Dioxide with the Surface of Zirconia Polymorphs. *Langmuir* **1998,** *14* (13), 3556-3564.

(28) Kouva, S.; Andersin, J.; Honkala, K.; Lehtonen, J.; Lefferts, L.; Kanervo, J., Water and Carbon Oxides on Monoclinic Zirconia: Experimental and Computational Insights. *Phys. Chem. Chem. Phys.* **2014,** *16* (38), 20650-20664.

(29) Ferretto, L.; Glisenti, A., Study of the Surface Acidity of an Hematite Powder. *J. Mol. Catal. A.* **2002,** *187* (1), 119-128.

(30) Si, R. R.; Liu, J. F.; Yang, K.; Chen, X.; Dai, W. X.; Fu, X. Z., Temperature-progamed Surface Reaction Study of CO Oxidation over Au/TiO_2 at Low Temperature: An Insight into Nature of the Reaction Process. *J. Catal.* **2014,** *311*, 71-79.

(31) Busing, W. R.; Morgan, H. W., Infrared Spectrum of $Ca(OH)_2$. *J. Chem. Phys.* **1958,** *28* (5), 998-999.

(32) Tennyson, J.; Bernath, P. F.; Brown, L. R.; Campargue, A.; Csaszar, A. G.; Daumont, L.; Gamache, R. R.; Hodges, J. T.; Naumenko, O. V.; Polyansky, O. L.; Rothman, L. S.; Vandaele, A. C.; Zobov, N. F.; Al Derzi, A. R.; Fabri, C.; Fazliev, A. Z.; Furtenbacher, T.; Gordon, I. E.; Lodi, L.; Mizus, II, IUPAC Critical Evaluation of the Rotational-Vibrational Spectra of Water Vapor, Part III: Energy Levels and Transition Wavenumbers for (H_2O)-O-16. *J. Quant. Spectrosc. Ra.* **2013,** *117*, 29-58.

(33) Sing, K. S. W.; Everett, D. H.; Haul, R. A. W.; Moscou, L.; Pierotti, R. A.; Rouquerol, J.; Siemieniewska, T., Reporting Physisorption Data for Gas Solid Systems With Special Reference to the Determination of Surface Area and Porosity (Recommendations 1984). *Pure Appl. Chem.* **1985,** *57* (4), 603-619.

(34) Sato, R.; Ohkuma, S.; Shibuta, Y.; Shimojo, F.; Yamaguchi, S., Proton Migration on Hydrated Surface of Cubic ZrO_2: Ab initio Molecular Dynamics Simulation. *J. Phys. Chem. C* **2015,** *119*, 28925-28933.

(35) Light, T. S.; Licht, S.; Bevilacqua, A. C.; Morash, K. R., The Fundamental Conductivity and Resistivity of Water. *Electrochem. Solid St.* **2005,** *8* (1), E16-E19.

(36) Scherrer, B.; Schlupp, M. V. F.; Stender, D.; Martynczuk, J.; Grolig, J. G.; Ma, H.; Kocher, P.; Lippert, T.; Prestat, M.; Gauckler, L. J., On Proton Conductivity in Porous and Dense Yttria Stabilized Zirconia at Low Temperature. *Adv. Funct. Mater.* **2013,** *23* (15), 1957-1964.

(37) Bauerle, J. E., Study of Solid Electrolyte Polarization by a Complex Admittance Method. *J. Phys. Chem. Solids* **1969,** *30* (12), 2657-2665.

(38) Guo, X.; Maier, J., Grain Boundary Blocking Effect in Zirconia: A Schottky Barrier Analysis. *J. Electrochem. Soc.* **2001,** *148* (3), E121-E126.

(39)   Avila-Paredes, H. J.; Chen, C.-T.; Wang, S.; De Souza, R. A.; Martin, M.; Munir, Z.; Kim, S., Grain Boundaries in Dense Nanocrystalline Ceria Ceramics: Exclusive Pathways for Proton Conduction at Room Temperature. *J. Mater. Chem.* **2010,** *20* (45), 10110-10112.

(40)   Avila-Paredes, H. J.; Zhao, J.; Wang, S.; Pietrowski, M.; De Souza, R. A.; Reinholdt, A.; Munir, Z. A.; Martin, M.; Kim, S., Protonic Conductivity of Nano-Structured Yttria-Stabilized Zirconia: Dependence on Grain Size. *J. Mater. Chem.* **2010,** *20* (5), 990-994.

(41)   Kim, S.; Avila-Paredes, H. J.; Wang, S.; Chen, C.-T.; De Souza, R. A.; Martin, M.; Munir, Z. A., On the Conduction Pathway for Protons in Nanocrystalline Yttria-Stabilized Zirconia. *Phys. Chem. Chem. Phys.* **2009,** *11* (17), 3035-3038.

(42)   Tande, C.; Perez-Coll, D.; Mather, G. C., Surface Proton Conductivity of Dense Nanocrystalline YSZ. *J. Mater. Chem.* **2012,** *22* (22), 11208-11213.

(43)   Bouchet, R.; Knauth, P.; Laugier, J. M., Theoretical Analysis of IS of Polycrystalline Materials with Blocking or Conducting Grain Boundaries: From Microcrystals to Nanocrystals. *J. Electrochem. Soc.* **2003,** *150* (7), E348-E354.

(44)   Bouchet, R.; Knauth, P.; Laugier, J. M., Theoretical Analysis of the Impedance Spectra of Electroceramics - Part 2: Isotropic Grain Boundaries. *J. Electroceram.* **2006,** *16* (3), 229-238.

(45)   Lacroix, O.; Rahmouni, K.; Sirat, A.; Takenouti, H.; Deslouis, C.; Keddam, M.; Sala, B., Electrochemical Studies of Water Insertion and Proton - Ceramic Interaction in Substituted Perovskite SrZr(0.9)Ln(0.1)O(2.95). *J. Power Sources* **2014,** *270*, 506-515.

(46)   Hwang, J. H.; McLachlan, D. S.; Mason, T. O., Brick Layer Model Analysis of Nanoscale-to-Microscale Cerium Dioxide. *J. Electroceram.* **1999,** *3* (1), 7-16.

(47)   Kidner, N. J.; Perry, N. H.; Mason, T. O.; Garboczi, E. J., The Brick Layer Model Revisited: Introducing the Nano-Grain Composite Model. *J. Am. Ceram. Soc.* **2008,** *91* (6), 1733-1746.

(48) Verkerk, M. J.; Middelhuis, B. J.; Burggraaf, A. J., Effect Of Grain-Boundaries on the Conductivity of High-Purity ZrO_2-Y_2O_3 Ceramics. *Solid State Ionics* **1982,** *6* (2), 159-170.

(49) Rojo, L.; Ga Mandayo, G.; Castano, E. Thin Film YSZ Solid State Electrolyte Characterization Performed by Electrochemical Impedance Spectroscopy, *9th Spanish Conference on Electron Devices (CDE), Valladolid, SPAIN*, **2013** Feb 12-14; Valladolid, SPAIN, 2013; pp 233-236.

(50) Hertz, J. L.; Tuller, H. L., Measurement and Finite Element Modeling of Triple Phase Boundary-Related Current Constriction in YSZ. *Solid State Ionics* **2007,** *178* (13-14), 915-923.

(51) Maeland, D.; Suciu, C.; Waernhus, I.; Hoffmann, A. C., Sintering of 4YSZ (ZrO_2+4 mol% Y_2O_3) Nanoceramics for Solid Oxide Fuel Cells (SOFCs), Their Structure and Ionic Conductivity. *J. Eur. Ceram. Soc.* **2009,** *29* (12), 2537-2547.

(52) Peters, C.; Weber, A.; Butz, B.; Gerthsen, D.; Ivers-Tiffee, E., Grain-Size Effects in YSZ Thin-Film Electrolytes. *J. Am. Ceram. Soc.* **2009,** *92* (9), 2017-2024.

(53) Obal, K.; Pedzich, Z.; Brylewski, T.; Rekas, M., Modification of Yttria-doped Tetragonal Zirconia Polycrystal Ceramics. *Int. J. Electrochem. Sc.* **2012,** *7* (8), 6831-6845.

(54) Wierzbicka, M.; Pasierb, P.; Rekas, M., CO_2 Sensor Studied by Impedance Spectroscopy. *Physica B-Condensed Matter* **2007,** *387* (1-2), 302-312.

(55) Tao, J.; Dong, A.; Wang, J., The Influence of Microstructure and Grain Boundary on the Electrical Properties of Scandia Stabilized Zirconia. *Mater. Trans.* **2013,** *54* (5), 825-832.

(56) Martin, M. C.; Mecartney, M. L., Grain Boundary Ionic Conductivity of Yttrium Stabilized Zirconia as a Function of Silica Content and Grain Size. *Solid State Ionics* **2003,** *161* (1-2), 67-79.

(57) Vishweswaraiah, S. Non-Destructive Micostructuarl Evaluation of Yttria Stabilized Zirconia, Nickel Aluminides and Thermal Barrier Coatings Using Electrochemical Impedance Spectroscopy. *PhD Thesis, University of Central Florida*, **2000**.

(58) Macdonald, J. R., *Impedance Spectroscopy - Theory, Experiment and Applications*. Wiley: New York, 1987; p page 191.

(59) Madani, A.; Cheikh-Amdounia, A.; Touati, A.; Labidia, M.; Boussetta, H.; Monty, C., Ionic Conductivity of 4 mol%, 9.5 mol% YSZ Nanomaterials and (9.5 mol% YSZ)(0.98)-(Al$_2$O$_3$)(0.02) Nanocomposites. *Sensor. Actuat. B-Chem.* **2005,** *109* (1), 107-111.

(60) Jung, W.; Hertz, J. L.; Tuller, H. L., Enhanced Ionic Conductivity and Phase Meta-Stability of Nano-Sized Thin Film Yttria-Doped Zirconia (YDZ). *Acta Mater.* **2009,** *57* (5), 1399-1404.

(61) Araki, W.; Imai, Y.; Adachi, T., Mechanical Stress Effect on Oxygen Ion Mobility in 8 mol% Yttria-Stabilized Zirconia Electrolyte. *J. Eur. Ceram. Soc.* **2009,** *29* (11), 2275-2279.

(62) Wang, Z. W.; Cheng, M. J.; Bi, Z. H.; Dong, Y. L.; Zhang, H. M.; Zhang, J.; Feng, Z. C.; Li, C., Structure and Impedance of ZrO$_2$ doped with Sc$_2$O$_3$ and CeO$_2$. *Mater. Lett.* **2005,** *59* (19-20), 2579-2582.

(63) Badenes, J. A.; Benet, P.; Sorli, S.; Tena, M. A.; Monros, G., Characterisation of Y-PSZ and Pr-doped Y-PSZ Obtained by Unconventional Methods for SOFC Applications. *Bol. Soc. Esp. Ceram. V.* **2004,** *43* (4), 787-791.

(64) Takamura, H.; Takahashi, N., Electrical Conductivity of Dense Nanocrystalline Ceria Under Humidified Atmosphere. *Solid State Ionics* **2010,** *181* (3-4), 100-103.

(65) Gong, J. H.; Li, Y.; Zhang, Z. T.; Tang, Z. L., AC Impedance Study of Zirconia Doped with Yttria and Calcia. *J. Am. Ceram. Soc.* **2000,** *83* (3), 648-650.

(66)   Tao, J. C.; Dong, A. P.; Wang, J., The Influence of Microstructure and Grain Boundary on the Electrical Properties of Scandia Stabilized Zirconia. *Mater. Trans.* **2013,** *54* (5), 825-832.

(67)   Fonseca, F. C.; Muccillo, R., Impedance Spectroscopy Analysis of Percolation in (Yttria-Stabilized Zirconia)-Yttria Ceramic Composites. *Solid State Ionics* **2004,** *166* (1-2), 157-165.

(68)   Miyoshi, S.; Akao, Y.; Kuwata, N.; Kawamura, J.; Oyama, Y.; Yagi, T.; Yamaguchi, S., Water Uptake and Conduction Property of Nano-Grained Yttria-Doped Zirconia Fabricated by Ultra-High Pressure Compaction at Room Temperature. *Solid State Ionics* **2012,** *207*, 21-28.

Table of content